Mapping and Analysis of Wrinkle Ridges in the Aeolis Dorsa Region, Mars: Implications for Stress Fields and Geologic Substrates

A Thesis Presented for the

Master of Science

Degree

The University of Tennessee, Knoxville

Rose Borden

December 2018

Copyright © 2018 by Rose M. Borden
All rights reserved.

ACKNOWLEDGEMENTS

Thank you to my advisor Devon Burr. I so appreciate your patience, love, and friendship throughout my grad school adventure. Your guidance through this project has been a wonderful blessing to me.

Many thanks also to my committee members – Josh, Bill, and Christian – for kind and helpful guidance on many aspects of this project and thesis. Special thanks to Josh. I am so thankful for your friendship these past years, for being willing to listen when I needed to talk about anything, and for making bomb mac and cheese.

Thanks also to the many folks in EPS who have provided help and encouragement throughout my journey here. Thank you to the wonderful ladies of the office staff for encouraging me to keep up the good work every day. To Cam H., for keeping us all sufficiently caffeinated. To the Paleo Crew (Jen, Sarah, and Maggie) for welcoming me as your token planetary scientist and putting up with my enthusiasm for extremely mundane fossils. To Joy and the rest of the ladies of 500 Women Scientists KnoxPod, for being a deep source of fellowship and encouragement.

To my Redeemer family, thanks for the community and love. It is such a blessing to care for your kids in the nursery and youth group and I have been so loved in return. Especially to the Hollis family (Pamela, Brian, Emily, and Daniel), your friendship has meant so much to me these last couple years. Thanks for all the hugs, meals, and opportunities to win at Rummikub!

To my home family, I know we have all missed each other being so far away but thank you for putting up with the distance and encouraging me to pursue my dreams. Love and hugs to all of you!!

ABSTRACT

Wrinkle ridges are tectonic geologic features found throughout the inner solar system. They are asymmetric, curvilinear ridges with a complex morphology interpreted to be due to deformation along thrust faults. Previous studies have mostly focused on large wrinkle ridges with maximum widths and lengths measuring tens and hundreds of kilometers, respectively. However, recent high-resolution data of the Martian surface have revealed small wrinkle ridges in the Aeolis Dorsa (AD) region along the global dichotomy boundary. Mapping and analyzing such small-scale wrinkle ridges can provide valuable information on tectonic processes operating at the regional or local scale. The null hypothesis driving this work is that wrinkle ridges in the AD region reflect regional deformation consistent with larger wrinkle ridges in the surrounding Cerberus plains and circum-Elysium region. Alternatively, they might reflect deformation that was more localized and different for different areas within AD. I derived information on shortening, strain, and principal stress directions in the AD region, as expressed by these small-scale wrinkle ridges. I mapped the locations of the wrinkle ridges using ArcMap software and created digital elevation models to determine their dimensions. Shortening due to folding was quantified based on the integrated lengths of topographic profiles and shortening due to faulting was derived from the differences in relief across the ridges and assumed dip angles. From each shortening estimate, I calculated values for strain. The geographic orientations were used to determine the principal stress directions. Cross-cutting relationships suggest formation postdated fluvial deposition and predated alluvial fan formation. The number of wrinkle ridges mapped in AD did not meet the minimum number required for a robust statistical test of clustering, but I visually identified several geospatially distinct clusters of wrinkle ridges. These clusters exhibited distinct orientations and amounts of strain. This result supports the alternate hypothesis of more than one stress field (or driver) operating in different locations, possibly simultaneously, during wrinkle ridge formation.

TABLE OF CONTENTS

Section 1: Introduction & Background 1

Introduction 1

Background 5

Wrinkle Ridges 5

Formation and Deformation Hypotheses 5

Terrestrial Analogs and Their Interpretations 6

Aeolis Dorsa Mapping Area 8

Section 2: Methods 11

Mapping of Wrinkle Ridge Locations 11

DEM Creation 12

Derivation of Topographic Profiles 13

Derivation of Shortening and Strain 14

Wrinkle Ridge Orientation 14

Clustering 14

Section 3: Results 15

Section 4: Analysis & Discussion 17

Suggestion of a Common Formation Process for Large and Small Wrinkle Ridges 17

Evidence for Four Geospatial Clusters of Wrinkle Ridges 17

Hypothesis Testing with Wrinkle Ridge Orientations and Strain Results 19

Chapter 5: Implications 22

Implications for Age 22

Northeast Cluster: Related to Tharsis Stress Field 22

Northwest Cluster: Not Related to Elysium or Tharsis 24

East Central Cluster: Evidence for Formation in Sedimentary Rock 25

Implications for Stratigraphy 27

Section 6: Conclusions **29**

Future Work *30*

List of References **31**

Appendix **45**

Steps for DEM Image Processing *46*

Figures and Tables *53*

Vita **80**

LIST OF TABLES

Table 1: Geologic settings and hypothesized formation mechanisms for wrinkle ridges on various planetary bodies. 57
Table 2: Criteria for determining certainty levels of wrinkle ridges. These criteria are compiled from the literature on wrinkle ridges, using the most commonly mentioned morphologic characteristics. 63
Table 3: Characteristics for each wrinkle ridge and the corresponding assigned certainty level, as well as characteristics of features originally mapped and then determined not to be wrinkle ridges (those without numbers). 71
Table 4: Wrinkle ridge orientations, certainty levels, locations, and dimensions. The height and width were measured for each profile across a ridge and the average value for each ridge is reported here. Estimated measurement error on height measurements is +/- 1 m, on width measurements is +/- 97 m, and on length measurements is +/- 362 m. N/A denotes wrinkle ridges for which no DEM was available. 73
Table 5: Results for calculations of shortening and strain from folding. Shortening results are in meters. Shortening was calculated by subtracting the straight-line length across each ridge from the integrated length of topographic profiles across that ridge. 75
Table 6: Results for calculations of shortening and strain from faulting. Shortening results are in meters. Shortening was calculated by dividing the elevation offset across a ridge by the tangent of the assumed fault dip (25º, 30º, or 35º, as indicated). 76
Table 7: Average strain and standard deviation for geospatial clusters of wrinkle ridges in AD 78

LIST OF FIGURES

Figure 1: Top: CTX DEM covering wrinkle ridge #4 in AD (for location, see Figure 5). The black line shows the location of the profile in the bottom image. The narrow crenulated ridge can be easily seen running NW-SE on the western side of the image and is pointed out by the red arrow. The broad arch is covered by the green double-sided arrow. Warm colors are high elevations and cool colors are low elevations. Scale bar is 5 km. Bottom: Topographic profile of wrinkle ridge #4. The blue arrow shows the low topographic rise, the red arrow shows the broad arch or hill, and the green arrow shows the narrow crenulation at crest. 54

Figure 2: (Left) Global map of Mars with colorized Mars Orbiter Laser Altimeter (MOLA) elevations, where warm colors are high and cool colors are low. Dashed line approximates the global dichotomy boundary. Black box with Elysium Mons and Cerberus Plains shows area of Figure 4. Black box around Solis Planum shows location of image at right. (Right) Large wrinkle ridges on Solis Planum. 55

Figure 3: Lobate scarp (indicated by dashed black line) in the southern highlands, located at approximately 117° E and 5° S.....56

Figure 4: Regional image of Elysium Mons and the Aeolis Dorsa region. Black lines show approximate locations of a sampling of wrinkle ridges near Elysium Mons. Black box shows location of Aeolis Dorsa study area (Figure 6). 58

Figure 5: Top: Image from Google Earth of several ridges in the Yakima Fold and Thrust Belt of central Washington state, a proposed terrestrial analog for wrinkle ridges on other planets (Reidel, 1984; Watters, 1988). Orange dashed lines show approximate trace of ridge crests. Bottom: Elevation profile of the Saddle Mountain anticline with topography taken from Shuttle Radar Topography Mission data is from A to A' (shown on top image). Colored arrows indicate the three morphologic parts of a wrinkle ridge: Blue arrows indicate edges of topographic rise, red arrows indicate broad arch or hill, green arrow indicates narrow crenulation at crest. 59

Figure 6: CTX mosaic basemap of Aeolis Dorsa study area with colorized MOLA elevations, where warm colors are high and cool colors are low. Aeolis and

Zephyria Plana are mapped as part of the Medusae Fossae Formation (MFF), a hypothesized ignimbrite or pyroclastic deposit. Black boxes show locations of images in Figure 8. 60
Figure 7: Images showing a wrinkle ridge deflecting an alluvial fan (left) and inverted fluvial deposits continuing across the same wrinkle ridge (right). Orange arrows show flow directions of alluvial fan deposit. Black lines show inverted fluvial deposits crosscutting a wrinkle ridge. This wrinkle ridge is located in the east central part of AD. This figure is similar to one in Kite et al. (2015). 61
Figure 8: Comparison of AD wrinkle ridge #4 (left) and inverted channel in SE AD (right) morphology. Colors show elevation, with cool colors as low elevations and warmer colors as high elevations. Wrinkle ridges have a more crenulated, irregular ridge morphology, while the inverted channels have a smoother but more branching morphology. This is the same wrinkle ridge as Figure 1. 62
Figure 9: CTX mosaic of the AD mapping area showing all wrinkle ridges mapped as well as coverage by CTX DEMs. For the DEMs, colors indicate topographic elevation, with orange and brown as higher elevations and green as lower elevations. Colored boxes show geospatial groupings, or “clusters”, of wrinkle ridges..... 64
Figure 10: All wrinkle ridges mapped as Certain. All scale bars are 2 kilometers. Colored outlines match colored boxes indicating clusters from Figure 9. 65
Figure 11: All wrinkle ridges mapped as Probable. All scale bars are 2 kilometers. Colored outlines match colored boxes indicating clusters from Figure 9 where applicable. 65
Figure 12: All wrinkle ridges mapped as Possible. All scale bars are 2 kilometers. Colored outlines match colored boxes indicating clusters from Figure 9. 66
Figure 13: AD study area showing locations of ridges determined not to be wrinkle ridges. These ridges are shown as red lines. See Table 3 for exact coordinates of these ridges. 67

Figure 14: All ridges in AD determined not to be wrinkle ridges using the characteristics in Tables 2 and 3. Ridges 18 and 28 are in the same image due to close proximity to each other. 68
Figure 15: An illustration of topographic profile lines, shown here for wrinkle ridge #4. The mapped wrinkle ridge line follows the crest of the ridge, although the profile lines were made much wider to capture the width of the broad arch and topographic rise. Yellow line marks location of profile line #8, shown below. See the Appendix for the location of topographic profiles on the other 11 wrinkle ridges for which I was able to derive CTX stereo-pair DEM data. 69
Figure 16: Graph of topographic profile #8 from Wrinkle Ridge #4. Orange line shows width measurement and green stars show lowest and highest points used for height measurement. The width for each ridge was measured as the straight line length between the point on either side of the ridge marking a change in slope. The height for each ridge was measured as the difference in elevation between the highest and lowest points on the ridge. 70
Figure 17: Example profile showing measurements used for shortening and strain calculations. Green line with arrows shows the measured straight-line width of the wrinkle ridge. The integrated length of the blue profile line is taken as the original width. The orange lines on either side of the wrinkle ridge mark the average elevation there; the difference between these two elevations is considered to be the elevation offset. The black line represents the assumed fault and fault dip underneath the ridge. 70
Figure 18: Rose diagram of all 19 wrinkle ridge orientations in AD, along with diagrams for the orientations of each geospatial cluster. Single-digit numbers on the concentric semi-circles of the diagram correspond to the number of wrinkle ridges within each 10º bin. 74
Figure 19: Heat map of wrinkle ridges made using Kernel Density tool in ArcMap. Darker blue colors mean there is a higher density of wrinkle ridges per area in that location. 77

Figure 20: Figure 10 from Hall et al. (1986) showing a stress map of the area south of Elysium Mons based on an isostatic model of Tharsis from Banerdt et al. (1982). Crosses show horizontal principal stress directions, arrows indicate extension. Contours show maximum stress difference in kilobars. 78
Figure 21: Image from just north of the AD study area showing WR 17 cutting across Aeolis Serpens (running from NW to SE across the image). 79

Section 1: Introduction & Background

Introduction

Wrinkle ridges (e.g., Figures 1, 2) are geologic features found throughout the inner solar system and commonly interpreted to be shortening structures (Plescia and Golombek, 1986; Schultz, 2000; Mueller and Golombek, 2004; Golombek and Phillips, 2010). They are curvilinear ridges in plan view with a complex morphology that in their most complete form include a low-relief topographic rise, a superposed hill or arch that constitutes the 'ridge' of the wrinkle ridges, and a narrow crenulation that constitutes the 'wrinkle' either on the top or to one side of the arch (Lucchitta, 1977; Golombek et al., 2001; Mueller and Golombek, 2004). Wrinkle ridges can also form polygonal or ring shapes, such as in Isidis Planitia on Mars (Head et. al., 2002; Mueller and Golombek, 2004). However, not all of these morphologic parts are present or visible on all wrinkle ridges, and some researchers instead recognize only the latter two parts as being sufficiently diagnostic of a wrinkle ridge (Watters, 1988; Schultz, 2000; Okubo and Schultz, 2004; Yue et al. 2015). Wrinkle ridges overall appear asymmetric: the ridges are steeper on one side than the other, although the sense of asymmetry may switch along strike (Watters, 1988). Wrinkle ridges often form as en échelon segments (Smart et al., 2006; Golombek and Phillips, 2010).

On Mars, wrinkle ridges are one of a number of diverse structural features that range from local to global in scale. The most global-scale structural feature on Mars is the dichotomy boundary (Figure 2), which is a large north-dipping escarpment that divides the southern highlands from the northern lowlands across much of the planet. This crustal dichotomy boundary is expressed as a single scarp in limited locations, and more generally manifests as a broad decline in crustal thickness and elevation within the cratered terrain between the thicker highlands and thinner lowlands crusts, and is also marked by knobs, mesas, and plateaus (Tanaka et al., 2003; Irwin and Watters, 2010; Golombek and Phillips, 2010; Tanaka et al., 2014). The dichotomy boundary has been associated with tectonic features at various locations, including contractional and extensional features in the eastern hemisphere (Watters, 2003a and 2003b; Nimmo,

2005; Lefort et al., 2015). However, some authors have suggested that these features do not have orientations that give evidence of any relation to the global dichotomy (Chicarro et al., 1985; Tanaka et al., 2014).

At the hemispherical scale, the most salient features are located in the Olympus Mons and Tharsis Montes province (Figure 2). Extensional structures occur near Tharsis and include radial rifts and graben caused by concentric extensional stress. Another large structural feature on Mars is Valles Marineris, a large canyon system to the east of the Tharsis province modeled to have formed by extension and vertical subsidence during the Late Noachian (Tanaka and Golombek, 1989; Andrews-Hanna, 2012a and 2012b; Tanaka et al., 2014). Shortening structures near Tharsis include concentric wrinkle ridges up to 400 kilometers long caused by radial compressional stress resulting from the growth of the Tharsis load (Figure 2b; Golombek and Phillips, 2010; Bouley et. al., 2018). Mars has other regional shortening structures in the form of lobate scarps, many examples of which are found in the ancient highlands of the eastern hemisphere (Watters and Robinson, 1999). Lobate scarps are large ridges that are interpreted to be the scarps of thrust faults that reach and rupture the surface. They are generally larger than wrinkle ridges (hundreds of meters to several kilometers in height), thus accommodating more shortening, and have a simple linear to arcuate asymmetric morphology (Figure 3; Mueller and Golombek, 2004; Golombek and Phillips, 2010, and references therein).

In addition to Mars, wrinkle ridges are found on all terrestrial planetary bodies in the inner solar system, including Mercury, Venus, Earth, and the Moon (See Table 1 for references). Although there are several hypothesized causes for wrinkle ridge formation in Table 1, all wrinkle ridges are generally interpreted to be developed as movement along blind thrust faults, in contrast to lobate scarps (Mueller and Golombek, 2004). However, like lobate scarps, they have been generally identified at the regional scale. For example, many Martian wrinkle ridges in Solis and Lunae Plana and marginal to the Cerberus lava plains (Figures 2 and 4) measure hundreds of kilometers along strike (Plescia and Golombek, 1986; Mueller and Golombek, 2004; Golombek and Phillips, 2010). Wrinkle ridges were also mapped throughout the northern lowlands by Head et al

(2002), who interpreted these ridges as completing a global circum-Tharsis pattern first noticed in Solis and Lunae Plana by Watters (1993). In data from the MESSENGER mission to Mercury, wrinkle ridges were observed in and around Caloris Basin and other craters filled with smooth plains material (Watters et al., 2009; Klimczak et al., 2012; Klimczak et al., 2013; Byrne et al., 2014). On the Moon, they are found mainly in the basaltic maria, although some can be traced to the highlands, and are hundreds of meters to many kilometers in length (Yue et al., 2015, and references therein). On Venus, they are found on large volcanic plains (Bilotti and Suppe, 1999). On Earth, they may be found near foreland fold-and-thrust belts (Figure 5; Golombek et al., 2001; Mueller and Golombek, 2004) in both sedimentary and igneous lithologies with layered stratigraphy and are tens of meters to ~150 kilometers in length (Table 1; Plescia and Golombek, 1986; Watters, 1988; Golombek et al., 2001). The Yakima fold-and-thrust-belt, considered the best and most-studied terrestrial analog (Watters, 1988), contains ridges that are ~100 kilometers long (Figure 5).

In addition to these regional examples, smaller wrinkle ridges, measuring one to two orders of magnitude shorter along strike, have recently been identified on multiple planetary bodies. Lunar wrinkle ridges with average widths and heights of 3.70 kilometers and 310 meters, respectively, are shown by recent mapping to have a global distribution (Yue et al. 2015). Small-scale wrinkle ridges (~50 kilometers in length) have also been identified in the Aeolis Dorsa region of Mars (Kite et al., 2015) just north of the global dichotomy boundary (Figure 6).

Due to limited high-resolution data, the morphology of wrinkle ridges at this smaller scale has not been examined in detail until recently (Yue et al., 2015). A global survey and analysis of lunar wrinkle ridges, including some at this smaller scale, resulted in an inference that small and large wrinkle ridges form by the same process (Yue et al. 2015). The small-scale wrinkle ridges in the AD region appear to be limited in number and extent, although there may be more wrinkle ridges than are currently visible due to the possibility of burial by sedimentary deposits in the region. However, mapping and analysis of these limited number of AD wrinkle ridges offers new information and insight into the local paleostress conditions at this one location along the dichotomy

boundary. Additionally, analyses of local wrinkle ridges along the dichotomy boundary will add to our understanding of the processes associated with the formation of this ubiquitous tectonic feature.

Beyond the potential to contribute to our understanding of stresses in proximity to the global dichotomy boundary, the AD wrinkle ridges may reflect regional conditions. Regional-scale wrinkle ridges are visible on the plains north of AD surrounding Elysium Mons and on the margins of the lava-filled Cerberus plains. These larger-scale examples have a generally NE-SW orientation (Figure 4), a regional orientation that suggests their formation in a single stress field. This stress field has been suggested to be related to Tharsis, as Elysium Mons is modeled to not be massive enough to produce a significant enough stress field to form these ridges (Plescia, 1986; Hall et al., 1986). If the smaller wrinkle ridges in AD show this same orientation, it would support the inference that they formed by the same stress field. However, if they have a different orientation than the larger wrinkle ridges or if they have multiple orientations, then they likely did not form from the same regional stress field but represent (a) different paleostress field(s).

For this work, the null hypothesis is that the Aeolis Dorsa wrinkle ridges reflect regional deformation. Evidence supporting this hypothesis would include i) wrinkle ridges with a single strong preferred orientation or with a pattern of orientations consistent with a single geographic location as the origin of deformation and ii) consistent strain values throughout the region. Alternatively, the wrinkle ridges could be the result of more localized deformation. Evidence supporting this hypothesis would be i) ridges across the AD region with orientations not following the regional structural trend and ii) variable strain values throughout the region. Either finding will provide new insight into the history of tectonic stress at the location. The results of testing these hypotheses also provide information on the AD substrate and on the similarity or difference of the formation mechanisms of large and small wrinkle rides on Mars.

Background

Wrinkle Ridges

Formation and Deformation Hypotheses

Although early work on Martian wrinkle ridges using images from the Viking spacecraft suggested volcanic or volcanotectonic origins (Plescia and Golombek, 1986), the current interpretation preferred by the community is that they are formed mainly by tectonic processes (Table 1; Mueller and Golombek, 2004; Golombek and Phillips, 2010). Evidence given in support of this interpretation is the common elevation offset on either side of the wrinkle ridge, interpreted as indicating a fault underneath the ridge, as well as the parallel orientation and regular spacing of wrinkle ridges in the ridged plains (Golombek et al., 1991).

Wrinkle ridges are commonly interpreted as evidence of contraction caused by blind thrust faults (Plescia and Golombek, 1986; Sharpton and Head, 1988; Golombek et al., 1991; Watters, 1988, 1991, and 1993; Watters and Robinson, 1997; Schultz, 2000). In this interpretation, wrinkle ridges are the topographic expression of fault-related folds developed by the thrusts. The resulting displacement gradient along the thrust fault causes fold formation in the hanging wall, creating the morphology seen at the surface, for which the kinematics are reviewed by Brandes and Tanner (2014).

Previous analyses of wrinkle ridges have resulted in a number of estimates for crustal shortening related to local and regional causes of deformation (e. g., Golombek et al., 1991; Plescia, 1991; Schultz, 2000; Golombek et al., 2001; Okubo and Schultz, 2004). One such study used topographic profiles across wrinkle ridges on the Moon and Mars to find the horizontal shortening due to folding, which was estimated by subtracting the straight-line length of each profile (current width of the ridge) from the integrated length of the profile (original width before horizontal shortening) (Golombek et al., 1991). The horizontal shortening due to faulting for that study was found by assuming a fault dip of 25° and dividing the elevation offset from one side of the ridge to the other by the tangent of that fault dip. The fault dip of 25° was derived as the complement of normal faults on Mars, which have an average measured dip of 65°, and

was also measured from sand box experiments in cohesionless material (Davis and Golombek, 1990; Golombek et al., 1991). Strain was then estimated using the total shortening from these two separate calculations. These estimates assume that shortening due to faulting as derived from surface elevation offset can be added together with that which occurs along the fault by displacement at depth for calculating strain, and that horizontal shortening is constant with depth for the fold-fault pair. Plescia (1991, 1993) used the same method to examine 25 wrinkle ridges on Lunae Planum and Golombek et al. (2001) examined wrinkle ridges throughout the ridged plains of Mars with the same method again when Mars Orbiter Laser Altimeter (MOLA) data became available. In contrast, Schultz (2000) reasoned that shortening due to folding measured at the surface is dependent on shortening due to slip along a related thrust fault at depth and because of this dependency the two types of shortening cannot be added to each other. This reasoning is based on the fact that the strain due to folding at the surface is influenced both by the depth to the fault tip and by the flexural slip offset along the fault. Accepting the Schultz (2000) model would mean that the two types of shortening could not be added together for estimating strain. This model, however, has been used in very few studies of wrinkle ridges (Cunje and Ghent, 2016; Li et al., 2018). Calculations of horizontal shortening due to faulting require an assumption of the fault dip, while calculations of horizontal shortening due to folding can be made using direct measurements of the width and integrated profile length of wrinkle ridges at the surface. Neither of these values is more important than the other, since they are different parts of an interrelated system. However, the ability to use direct measurements to calculate shortening from folding makes it a more direct and reproducible way to measure strain. For this work, I derive estimates of shortening from both faulting and folding and report them separately.

Terrestrial Analogs and Their Interpretations

In the absence of in situ field data about planetary wrinkle ridges, terrestrial analogs have been useful for inferring the processes and conditions contributing to wrinkle ridge formation. Several areas on Earth, where ridges have been formed by

thrust fault-related folding, have been proposed as terrestrial analogs for planetary wrinkle ridges. These analogs include ridges formed by fault-related folding on several different continents and occur within both sedimentary and igneous lithologies (e.g., Plescia and Golombek, 1986; Watters, 1988 and 1989; Golombek et al., 2001; Casale and Pratt, 2015). Some of these terrestrial faults break the surface and others result only in folding above the fault.

The most well-studied terrestrial analog ridges for planetary wrinkle ridges are the ridges of the Yakima Fold and Thrust Belt (YFTB) in the Columbia River Basalt Province (Figure 5; Reidel, 1984; Plescia and Golombek, 1986; Watters, 1988 and 1989; Casale and Pratt, 2015). The YFTB includes several ridges in central Washington state that are sub-parallel and periodically spaced (Figure 5; Watters, 1989). The Columbia River basalt contains thin sedimentary interbeds, thought to be due to streams and drainage systems established in between lava eruptions, with a primarily siliciclastic and volcaniclastic lithology that result in mechanical strength discontinuities (Reidel et al., 1989). These sedimentary layers have been modeled to act as free slip surfaces (Watters, 1989). Under compression, this alternating of strong and weak layers results in elastic buckling of the rock, eventually leading to plastic yielding of the basalt to form the asymmetric ridge shape. The deformation leading to the ridge formation in the YFTB is due to the Olympic-Wallowa Lineament (OWL), a fault running from the Olympic Peninsula in northwestern Washington state southeast to the northeastern corner of Oregon. The overall clockwise rotational motion in the Pacific Northwest resulting in the OWL and related deformation is inferred to be due to the motion of the Pacific plate subducting obliquely underneath the North American plate (Reidel, 1984).

Other terrestrial analogs suggested by Plescia and Golombek (1986) include deformation from thrust faults in Meckering, Australia; El Asnam, Algeria; Buena Vista Hills, California; and Alae Crater, Hawaii. Of these potential analogs, Watters (1988) concurs that the Buena Vista Hills and El Asnam structures are good analogs for planetary wrinkle ridges on the basis of comparable scales. One of the conclusions of the Watters (1988) discussion of terrestrial analogs is the inference that, although many observed wrinkle ridges on planetary bodies are in layered basalt flows, wrinkle ridges

can form in other layered lithologies if there are large strength contrasts between the layers (Plescia and Golombek, 1986; Watters, 1988). These strength contrasts allow for slip between the layers resulting in wrinkle ridge formation (Watters, 1988).

Aeolis Dorsa Mapping Area

The study area for this work is the Aeolis Dorsa (AD) region, the westernmost part of the Hesperian-Amazonian transitional unit (AHtu; Tanaka et al., 2014) associated with the dichotomy boundary. This study area was selected as part of a USGS geologic mapping project funded by a NASA grant focused on the many inverted fluvial features found in the region (Jacobsen and Burr, 2018). Located south of Elysium Mons and the Cerberus lava plains and extending to the Tharsis bulge, this transitional terrain, also known as the Medusae Fossae Formation (MFF), is hypothesized to be a volcanic ignimbrite based on morphologic (e.g., layering and yardangs) and physical characteristics (e.g., low density) (Scott and Tanaka, 1982 and 1986; Tanaka, 2000; Mandt et al., 2008; Ojha et al., 2017). The MFF is heavily eroded by aeolian abrasion as evidenced by pervasive yardangs (Ward, 1979; Wells and Zimbelman, 1997; Kerber and Head, 2010). The numerous inverted features, such as impact craters (Pain et al., 2007) and fluvial deposits (e.g., Burr et al., 2009; Kite et al., 2015; Jacobsen and Burr, 2017), likewise attest to wide-spread exhumation. This wide-spread erosion and exhumation is evidence of the complicated stratigraphic history in this region.

Previous studies in AD have attempted to constrain the timing of various events and have divided the stratigraphy into several units based on age (Kite et al., 2015; Jacobsen and Burr, 2017; Jacobsen et al., 2018). The most relevant finding for this project is the inference from Kite et al. (2015) that the wrinkle ridges in AD are younger than inverted river channel deposits but older than inverted alluvial fan deposits. This inference is based on wrinkle ridges appearing to cross-cut some of the inverted channel deposits but deflecting some inverted alluvial fan deposits (Figure 7).

Within the AD mapping area (Figure 6), the largest physiographic features include Aeolis and Zephyria Plana, located in the western and northeastern portions of

the study area, respectively. Between these plana is a broad central basin and in the southern study area is a more confined and deeper depression.

Previous mapping in the study area has identified several types of small-scale ridge features formed by a variety of processes. The Aeolis Dorsa themselves are an extensive population of sinuous ridges, generally interpreted as inverted fluvial deposits (Burr et al., 2009; Williams et al., 2013; Kite et al., 2015; Jacobsen and Burr, 2017). These fluvial deposits with different morphologies and degrees of inversion are observed most commonly distributed around the margins of Aeolis and Zephyria Plana, although the longest inverted paleochannel in the region, known as Aeolis Serpens, trends approximately NW-SE through the central basin. Alluvial fans are located preferentially in the northwest of the map area, where their morphology suggests formation by sheet floods, and in the southeast, where their morphology implies debris flow formation (Jacobsen and Burr, 2017). Aeolian features occur as sand deposits (Burr et al., 2011 and 2012; Boyd and Burr, 2017 and 2018) and on the plana surfaces as erosional yardangs (e. g., Ward, 1979; Wells and Zimbelman, 1997), which can exhibit a sinuous ridge morphology. The largest impact craters have rampart ejecta, suggesting impact into volatile-rich target material (Kerber and Head, 2010), which can exhibit sinuous positive-relief margins. Lastly, intracrater units that may indicate lacustrine deposition have a sinuous ridged appearance (Peel and Burr, 2018). Thus, the AD region exhibits various linear or curvilinear ridge morphologies of multiple origins – fluvial, aeolian, impact, lava flow fronts – of which the tectonic wrinkle ridges constitute just one genetic type.

Among these various features, the AD region contains several features that imply tectonic deformation. The shape of the global dichotomy boundary in this region has been modeled as consistent with lower crustal flow (Nimmo, 2005). The model used by Nimmo (2005) predicts compression to the south of the dichotomy boundary and parallel to it, extension just to the north, also parallel to the boundary, and minor compression to the north of the boundary as well. Some observations of the region (Watters, 2003a) appear to match that model. For example, lobate scarps (Figure 3) are located to the south of the global boundary in the southern highlands. In addition, the

large southern depression mentioned in the previous paragraph and located just to the north of the dichotomy boundary in AD, is modeled to be extensional.

No compressional features have been observed parallel to the boundary on the northern side (Nimmo, 2005). However, a close examination of the along-strike slopes of deformed surficial fluvial deposits in AD revealed that they undulate along-strike. This observation is consistent with lithospheric flexure due to erosion of the southern highlands and deposition of that material in the northern lowlands, although this flexure may have occurred at a later time (Lefort et al., 2015).

Another transitional unit, just to the west of the Medusae Fossae Formation, contains rectilinear troughs, also known as “fretted terrain”, potentially formed by erosion along preexisting tectonic fractures (Irwin et al., 2004) and appearing in the southwest of the AD region, both within and outside the map area. More locally, several wrinkle ridges were previously identified in the southeast part of the map area and were interpreted to have deflected, and thus predate, alluvial fan deposits (Kite et al., 2015). These previously identified wrinkle ridges have a preferred orientation (NNE-SSW), exhibit topographic asymmetry (steeper on one side), and are more linear with more rugged surface topography than the flat-topped inverted channels also seen in AD (Figure 8; Kite et al., 2015).

Section 2: Methods

The methods used to collect data for this project include mapping the wrinkle ridges in ArcMap using spacecraft images and elevation data, measuring the geographic orientations of the ridges to determine any modal orientations, and deriving topographic profiles of the wrinkle ridges from digital elevation models (DEMs) to measure wrinkle ridge dimensions and estimate shortening and strain. In determining the most applicable methods for this data collection, I assessed the relevant methods reported in the literature and used those that were most clearly elucidated and reproducible. Another consideration was the usability of the technique in this heavily eroded and exhumed landscape.

Mapping of Wrinkle Ridge Locations

The first step of this project was mapping the location and length of each wrinkle ridge in the AD mapping area using ESRI's ArcMap Geographic Information System (GIS) software. The basemap was a mosaic of Mars Reconnaissance Orbiter (MRO) Context Camera (CTX) images (Malin et al., 2007). CTX images have a 5-6 m/pixel resolution (Malin et al., 2007), which means they can be used for mapping features of the size of the small-scale wrinkle ridges, and nearly 100% coverage in AD. To assist with mapping, topographic data from the Mars Orbiter Laser Altimeter (MOLA; Smith et al., 2001) were overlain on the CTX mosaic, causing ridge crests to be more visually distinguishable. I identified possible wrinkle ridges by systematically examining the whole study area and marking, as potential wrinkle ridges, features that exhibited similar characteristics to previously described wrinkle ridges.

As discussed above, the map area exhibits a number of types of sinuous ridges, such as lava flow fronts, edges of crater ejecta, and inverted fluvial channel deposits (Burr et al., 2009; Kite et al., 2015; Jacobsen and Burr, 2017). To distinguish wrinkle ridges from these other types of ridges and to help promote accurate mapping, I created a rubric showing the most commonly agreed-upon wrinkle-ridge characteristics (Table 2). Four of these characteristics are best seen in plan view: a narrow crenulated ridge, en échelon segments, curvilinear shape, and a broad arch. Two of these characteristics

are more easily seen in profile data: a low topographic rise and asymmetry. I then created DEMs (see DEM Creation section below and Appendix) and visually evaluated each possible wrinkle ridge in images and topographic profiles from the DEMs using these six characteristic criteria compiled from the literature. Based on the number of discernable characteristics, the wrinkle ridge was assigned a qualitative certainty level of Certain, Probable, or Possible (Tables 2 and 3; Figures 9-12). I used these criteria to help identify the wrinkle ridges in this heavily eroded landscape and to reproducibly distinguish between wrinkle ridges and the other linear or sinuous ridge features. The resultant certainty levels indicate my confidence in this distinction and interpretation of the features as wrinkle ridges, but were not used for individual analyses. That is, all mapped wrinkle ridges were included in my analyses.

DEM Creation

Once mapping was completed, I created DEMs from overlapping stereo pair images for the 12 AD wrinkle ridges for which stereo pair images were available (see Appendix) from the Context Camera (CTX) images on the Mars Reconnaissance Orbiter (MRO). High Resolution Imaging Science Experiment (HiRISE) images, also from the MRO, have higher resolutions, but do not cover any of the mapped wrinkle ridges in Aeolis Dorsa.

The Planetary Image Locator Tool (PILOT; https://pilot.wr.usgs.gov/) from the USGS was used to identify and download CTX stereo pair images of wrinkle ridges in AD. The Imaging Software for Imagers and Spectrometers (ISIS) was used to add latitude and longitude data to the images, to radiometrically correct them, and to map project them. After processing, I merged the images into a DEM using the Ames Stereo Pipeline software (Moratto, 2010). The result was eight CTX DEMs covering 12 of the wrinkle ridges in AD (Figure 9; Appendix) with resolutions ranging from 5.33-6.11 meters per pixel. One High Resolution Stereo Camera (HRSC) image covers an AD wrinkle ridge, but that image is redundant with a CTX image stereo pair and has a lower resolution, so it was not used.

Derivation of Topographic Profiles

To obtain topographic profiles, I first uploaded each DEM into ArcMap and created a new polyline shapefile layer for each wrinkle ridge. I then drew approximately 30 profiles as shapefile lines across each wrinkle ridge (Figure 15 and Appendix), added the topographic information from the corresponding DEM to the shapefile lines using the Interpolate Shape tool in ArcMap, and exported the topographic profile data to .csv files for analysis. I used 30 profile lines wherever possible to enable statistical comparisons. In some cases the wrinkle ridges were so small that 30 lines were not possible due to the resolution of the drawing tool in ArcMap. However, even if there are not the 30 profiles needed for robust statistical comparisons, the data from the wrinkle ridges can still be compared with each other qualitatively and can be a starting place for future investigations.

These profile data enabled me to measure the height and width of each ridge (Table 4). The width of each wrinkle ridge was measured as the distance between the points on either side of the ridge where there were clear slope breaks, indicating the lateral edges of the wrinkle ridge. Watters (1988) defines the height of a wrinkle ridge as "the difference between the maximum elevation on the profile and the average elevation level beyond the major inflection points marking the lateral limits of the feature". In contrast, Golombek et al (1991) define wrinkle ridge height for lunar structures as "the difference in elevation between the point marking the change in slope between the broad rise and the lower mare surface and the highest point on the ridge". For this project, I used the Golombek et al. method, because the key features for the Watters (1988) approach were difficult to discern, due to the presence of yardangs and small craters located on or adjacent to the ridge.

Widths are reported only for the 12 wrinkle ridges with DEM coverage. All profiles obtained over each ridge were examined and compared to each other and to the map view on the DEM covering that ridge to determine the most likely location along the profile of the lateral edges of the ridge (see Figures 16 and 17 for example profiles). The average height and width of each ridge is reported here and can be compared to previous studies which often also reported average values (Table 4; Watters, 1988;

Golombek et al., 1991; Plescia, 1993; Mangold et al., 1998). The error for the measurements listed in Table 4 is the standard deviation for each type of measurement.

Derivation of Shortening and Strain

As explained in the background, I calculated the shortening and strain due to folding and faulting separately (Figure 17), following the approach of Golombek et al. (1991). I determined the shortening from folding by subtracting the straight-line width of each ridge from the integrated length of the topographic profiles over each ridge. the shortening from faulting was computed by dividing the difference between the elevations at the maximum lateral extents of the ridge by the tangent of the assumed fault dip. This calculation was completed for assumed fault dips of 25°, 30°, and 35°, a range used to accommodate the range of likely fault dips on Mars (Golombek et al., 1991). The strain for each of these types of shortening was calculated by dividing the shortening by the integrated length of the topographic profiles over each ridge.

Wrinkle Ridge Orientation

The geographic orientation of each wrinkle ridge was measured in ArcMap using the Add Geometry Attributes tool in the Data Management toolbox. These orientations were then input into the GeoRose software program (Yong Technology Inc., 2014) to produce a rose diagram. The orientations were binned in increments of 10^{o} starting at 0^{o} (north).

Clustering

After mapping was completed, a visual inspection of the locations of wrinkle ridges in AD revealed several possible geospatial “clusters” of wrinkle ridges. A heat map was produced using the Kernel Density tool in ArcMap to give an objective visual representation of this observation. This tool calculates the density of point or line features per area using a kernel function. The heat map has darker shading in places where features have a high density per unit area, and lighter shading where there are fewer features per unit area. The kernel function used for this tool is based on the quartic kernel function in Silverman (1986).

Section 3: Results

Mapping of wrinkle ridges in AD resulted in 19 identified wrinkle ridges: three Certain, twelve Probable, and four Possible (Table 3; Figures 9-12). All three of the Certain ridges, eight of the twelve Probable ridges, and one of the four Possible wrinkle ridges have full or partial DEM coverage. Although the DEMs do not cover all of the mapped wrinkle ridges in AD, this lack of full coverage should not bias the results because the DEMs do cover ~72% of the mapped length of wrinkle ridges distributed throughout the area, at different elevations and in different lithologies. These 12 ridges with DEM coverage were measured to find width and height dimensions and amounts of shortening and strain. The common wrinkle ridge characteristics were used to examine all features mapped as potential wrinkle ridges and eliminate those that do not meet the criteria to be considered wrinkle ridges (Tables 2 and 3; Figures 13 and 14).

The geographic orientations of these ridges were exported from ArcMap and graphed as a rose diagram (Figure 18; see also Table 4). This diagram shows that the wrinkle ridges are largely oriented within a constrained range from NW-NE (between 330° and 50°), with a single ridge oriented outside of this range (in the 60-70° bin).

The length, average width, and average height for each wrinkle ridge are recorded in Table 4 (see also Figure 16). The lengths for all 19 mapped wrinkle ridges ranged from 2.2 kilometers to 46 kilometers, although several wrinkle ridges in the northeast corner of the map area extend beyond the limits of the study area, and thus their lengths are minimum values. For the 12 wrinkle ridges with DEM coverage, the widths ranged from 0.5 kilometers to 10.5 kilometers, and the heights ranged from 16 meters to 141 meters.

The shortening and strain calculation results are recorded in Tables 5 and 6, showing that the average shortening due to folding ranges in the tens of meters, whereas average shortening due to faulting is greater as a function of the selected dip angle for the proposed subsurface thrust fault. These faults are not visible at the surface, meaning the dip angles are only estimated. The corresponding strains for folding range in the tenths of percent. The strains from faulting are the same order of

magnitude, with slightly greater values associated with the lower dip angles. There seemed to be no preference where along the strike of each wrinkle ridge the maximum shortening occurred. For WR #s 4, 5, 6, 7, 17, and 20 the maximum shortening from faulting value occurs closer to one end of the mapped length of the ridge than the middle of the length of the ridge.

The results of the Kernel Density tool run in ArcMap show that there are concentrations of wrinkle ridges in several places throughout AD, supporting the visual observations (Figure 19).

Section 4: Analysis & Discussion

Suggestion of a Common Formation Process for Large and Small Wrinkle Ridges

The results of the mapping and profile measurements can be used to compare the wrinkle ridges in AD to wrinkle ridges in other areas on Mars. The lengths of wrinkle ridges in AD (Table 4), which range from ~2 to 46 kilometers, are up to two orders of magnitude shorter than those on the ridged plains of Mars (Solis and Lunae Plana) and around the Tharsis rise, which are tens to hundreds of kilometers long (Plescia and Golombek, 1986; Golombek et al., 2001). The widths of wrinkle ridges in AD, which range from ~750 meters to ~40 kilometers, overlap at their largest sizes with the narrowest ridges on the ridged plains (Plescia and Golombek, 1986; Watters, 1988; Plescia, 1991; Golombek et al., 1991; Watters, 1993; Schultz, 2000; Mueller and Golombek, 2004). The heights of wrinkle ridges in AD, between ~20-160 meters, are within the small end of the range of those on the ridged plains, which are 20-500 meters high (Plescia and Golombek, 1986; Watters, 1988; Plescia, 1991; Golombek et al., 1991; Golombek et al., 2001; Mueller and Golombek, 2004).

Thus, in all three dimensions, the AD wrinkle ridges overlap and form a continuum with the larger Martian wrinkle ridges on the ridged plains. Yue et al. (2015) interpret a continuum of width-height ratios for lunar wrinkle ridges as implying that large and small wrinkle ridges on the Moon formed by the same process (blind thrust fault) and that larger wrinkle ridges simply represent more shortening. This means that, while the source of stress or timing of formation may be different for different ridges, the underlying fault geometry is thought to be the same. By the same reasoning, the continuum in dimensional sizes for the AD wrinkle ridges suggests a common formation process for both large and small wrinkle ridges on Mars.

Evidence for Four Geospatial Clusters of Wrinkle Ridges

I visually inspected the mapped wrinkle ridges in Aeolis Dorsa for possible areas of clustering and found 4 such areas. The existence of these clusters is further supported by the results of the Kernel Density tool (Figure 19). The first area is in the

northwest part of the AD study area (purple box in Figure 9). This cluster consists of four wrinkle ridges (1,4,17,23) that are all located in low-albedo, smooth terrain that retains small (kilometer-scale) impact craters (Jacobsen and Burr, 2018). The terrain also contains a few inverted impact craters with ejecta morphologies that indicate the past presence of overlying MFF (Kerber and Head, 2010). This low-albedo terrain is interpreted as exposed Hesperian or Amazonian lava (Kerber and Head, 2010; Jacobsen and Burr, 2018). The wrinkle ridges in this part of the study area all have a NNW orientation, indicating shortening in approximately the E-W direction (Figure 18). The certainty levels of these wrinkle ridges are all ‘certain’ or ‘probable’, indicating good preservation of morphology. This good preservation could be due to an erosion-resistant host lithology and/or to recent formation or exposure ages.

A second cluster, also consisting of four wrinkle ridges (3,15,19,20), occurs in the northeastern part of the study area (green box in Figure 9), to the northeast of Zephyria Planum. As in the northwest cluster, the terrain unit that hosts the wrinkle ridges is low-albedo and retains small impact craters. This terrain is mapped in Tanaka et al. (2014) as Hesperian-aged lava plains (Berman and Hartmann, 2002). The wrinkle ridges in this second cluster have a NE-SW orientation (Figure 18), indicating shortening in a slightly rotated direction from the first cluster. This difference in orientation from the northwest cluster is consistent with the visual identification of these wrinkle ridges as a geospatially separate cluster. None of these wrinkle ridges has a ‘certain’ classification, suggesting less distinct initial morphologies or poorer preservation than the ridges in the northwestern cluster.

A third possible cluster is in the central eastern part of the study area (orange box in Figure 9). The five wrinkle ridges (5,6,7,8,21) in this cluster are also mentioned in Kite et al. (2015), who interpret them as having deflected the alluvial fans nearby. The lithology underlying these wrinkle ridges is uncertain because there are many other geologic features in this area – such as inverted fluvial channels, alluvial fan deposits, and impact craters with ejecta blankets – covering up the underlying lithology. The orientation of these ridges is between those of the northern two clusters and indicates

shortening in the WNW-ESE direction (Figure 18). Their certainty levels range from ‘certain’ to ‘probable.’

A fourth possible cluster, consisting of three wrinkle ridges (14,24,26), is in the far southeastern corner of the study area (red box in Figure 9). A gap in CTX coverage in this area and lack of DEMs limit inferences about the host lithology. As in the northeastern cluster, none of these wrinkle ridges has a ‘certain’ classification. There are no shortening or strain estimates for these ridges due to the lack of DEM coverage.

Two of the remaining wrinkle ridges are located on blocks of material that are thought to be older and possibly remnants of the southern highlands bedrock (Jacobsen and Burr, 2018). The final wrinkle ridge, also mapped by Kite et al. (2015), is located within a crater in the medial basin between Aeolis and Zephyria Plana. The larger (~10-110 kilometers) craters in this sedimentary basin exhibit a variety of units, all of which are interpreted to be sedimentary (Peel and Burr, 2018), implying that this wrinkle ridge, classified as ‘possible’, formed in a sedimentary unit.

Hypothesis Testing with Wrinkle Ridge Orientations and Strain Results

The results of this project indicate that wrinkle ridges in the Aeolis Dorsa region do not have a single strongly preferred orientation but do have a confined range approximately NW-NE, between 330° and 50° (Figure 18). They are not randomly distributed, but they do have several distinct orientation groupings throughout the region. This result implies that, although the maximum compressive stress seems to have been oriented generally in the E-W direction rather than in the N-S direction, there was also some variation in the direction of the maximum principal stress over the time of wrinkle ridge formation. Thus, the data from this study more strongly support the alternate hypothesis, which states that wrinkle ridges in AD formed under multiple different stress fields, than the null hypothesis, which states that they formed due to a single stress field.

The strain also varies throughout the AD region. Table 7 contains the average strain and standard deviation for the three clusters with DEM coverage. For the NW and central clusters, the average strains from folding are similar (within 0.002), but the

standard deviation for both is larger than the mean, indicating a wide spread in the data for these clusters. The average strain from folding for the NE cluster is much smaller. The strain from faulting average values are all smaller than their standard deviations, again indicating a wide spread in the data, although there is also a bigger difference in the values between different clusters than with the strain from folding (0.02 rather than 0.013). The variable strain values throughout the AD region are weakly consistent with the orientation data in supporting different stresses in different parts of AD.

It would be expected that the maximum shortening would occur near the middle of the length of each ridge, since strain should increase toward the center of a shear zone (Fossen, 2010). Therefore, the result showing that maximum shortening sometimes occurs closer to one end of any particular ridge rather than the middle could be biased by the fact that several ridges may have been subject to burial or erosion and thus the length exposed today may not be their full original length. This possible burial or erosion could mean that the maximum shortening might actually occur near the middle for all ridges, but is unable to be seen with the current exposure of wrinkle ridges in AD. The only wrinkle ridge identified in this study with maximum shortening closer to one end than the other for which there is visual evidence of possible burial is #4 (Figures 1 and 15).

Burial of wrinkle ridges by subsequent deposition of sediment is a possibility in AD. There have been no wrinkle ridges mapped on Aeolis and Zephyria Plana in AD, which are part of the Medusae Fossae Formation (MFF). In fact, WR #4 can be seen possibly continuing underneath Aeolis Planum (Figures 1 and 15). If the deposition of the MFF resulted in the burial of multiple wrinkle ridges, then the present geographic distribution would not represent the total amount of shortening that has occurred in the area. Burial of wrinkle ridges would also imply that the clusters that have been identified in this study may not be so isolated.

The general east-west orientation of the contraction is unexpected, as the global dichotomy boundary is oriented roughly northwest-southeast in this location. Paleostresses were inferred to have been transverse to this boundary (slightly northeast-southwest) by two previous studies based on the orientations of tectonic

features parallel to the boundary (e.g., Nimmo, 2005; Lefort et al., 2015). These paleostresses are inferred to have been caused by lateral crustal flow beneath the dichotomy boundary here (Nimmo, 2005; Lefort et al., 2015). Thus, the orientations of the wrinkle ridges identified in this study as roughly perpendicular to the boundary are unexpected because they are opposite of the previous results.

Chapter 5: Implications

Implications for Age

The wrinkle ridges in the northwest and northeast clusters must be younger than the estimated age of the lava flows in which they are found, which gives a maximum for their estimated age. For the northwest cluster, the age of those lava flows is Hesperian (Kerber and Head, 2010). For the northeast cluster, the lava flows are part of the Cerberus plains and are late Hesperian/Amazonian (Berman and Hartmann, 2002). The ridges in the east central cluster can be seen deflecting alluvial fan deposits (Figure 7), indicating they are older than those deposits, although the ages of those alluvial deposits are currently uncertain. Older inverted fluvial channel deposits have been traced across the wrinkle ridges, meaning the wrinkle ridges are younger than those inverted deposits (Kite et al., 2015). This conclusion implies that the wrinkle ridges in this cluster formed in the time period between formation of the older channel deposits (suggested to be Noachian; Burr et al. 2016) and the younger fan deposits (of unknown age). According to Kite et al. (2015), the alluvial fan deposits and wrinkle ridges were likely formed during the Hesperian. These different possible ages for the clusters of wrinkle ridges in AD (Hesperian in the NW, late Hesperian/Amazonian in the NE, and Noachian to Hesperian for the central cluster) add more support to the conclusion of this study that there have been several stress fields over time and throughout the region, as stated in the alternate hypothesis.

Northeast Cluster: Related to Tharsis Stress Field

The wrinkle ridges in the northeast cluster (green box on Figure 9) oriented NE-SW continue off the map to the northeast. For context, I used the Thermal Emission Imaging (THEMIS) daytime infrared data mosaic (Christensen et al., 2004) to examine the landscape surrounding this corner of the map area. This examination showed these AD wrinkle ridges to be part of a population of subparallel wrinkle ridges to the northeast of AD, possibly related to a larger population of wrinkle ridges marginal to the Cerberus plains and Elysium Mons. These circum-Cerberus wrinkle ridges are ~20-40 kilometers

wide and ~100-220 kilometers long in plan view, although this length dimension is likely an underestimate, as the ridges disappear at the margin of the Cerberus plains (Figure 4), interpreted as very late Amazonian lava (Keszthelyi et al., 2000 and 2004; Jaeger et al., 2010; Vaucher et al., 2009). The host unit for these AD wrinkle ridges in the northeast corner of the study area is Hesperian-age lava (Tanaka et al., 2014 map).

The ridges in AD located to the southeast of Elysium Mons are roughly concentric to Elysium Mons (Figures 2 and 4), whose most recent lavas are also Hesperian in age (Tanaka et al., 2014). However, other wrinkle ridges in the region to the northeast and southwest of Elysium outside the study area are oriented radial or sub-radial to Elysium Mons (Figure 4). The orientations of all of these wrinkle ridges in the region of Elysium match a stress map (Figure 20) produced by Hall et al. (1986) from an isostatic model of Tharsis based on Banerdt et al. (1982). Although this model does not extend south as far as the AD map area, it stops just north of the map area and thus can be used to estimate the approximate stress direction in the AD area. The stress field produced by loading by Elysium Mons may have exerted some influence on the orientation of these wrinkle ridges (Hall et al., 1986). However, Elysium Mons itself would not have been a sufficient load to produce the number and size of wrinkle ridges seen in this region (Hall et al., 1986). The wrinkle ridges surrounding Elysium also exhibit a range of orientations not consistent with an origin at Elysium (Hall et al., 1986). As suggested by the apparent concentric-to-Tharsis orientations of the ridges in this cluster, a larger stress field influenced by Tharsis likely existed at the time of wrinkle ridge formation.

Given the host lithology, another option for wrinkle ridge formation could be contraction during lava cooling (Strom et al., 1975; Solomon et al., 2008). An analog for this process is the wrinkle ridges in the lunar maria (Watters, 1988; Golombek et al., 1991; Watters and Johnson, 2010). However, a global study of lunar wrinkle ridges concluded that a volcanic origin alone is unlikely and that other tectonic stresses are necessary (Yue et al., 2015).

Wrinkle ridges formed from global contraction would likely have random orientations, unlike the wrinkle ridges in AD (Watters et al., 2001 and 2004). However,

given the similar orientations of the wrinkle ridges in this cluster to those expected from the figure in Hall et al. (1986) showing stress directions due to Tharsis (Figure 20), the wrinkle ridges in this cluster likely formed from stress related to Tharsis loading. The inferred ages of these wrinkle ridges (late Hesperian/Amazonian) are consistent with an origin related to Tharsis as well, based on a recent analysis of tectonic structures surrounding Tharsis by Bouley et al. (2018) which found a peak of compressional tectonism around the early Hesperian, but a large percentage of structures which formed during the late Hesperian/Amazonian as well. Thus, some regional stress field (or fields) is (are) also a likely component in the formation of these wrinkle ridges in the northeast corner of the map area, since they have sub-parallel (not random) orientations.

The strain of these wrinkle ridges is also consistent with the explanation of a formation by a Tharsis-related stress field. Average strain related to global contraction on Mars calculated from wrinkle ridges ranges from 0.00011-0.00022 (Nahm and Schultz, 2011). This strain is lower than the average strain calculated for the wrinkle ridges in this cluster (Table 7). Golombek et al. (2001) calculated strain across ridges in the Tharsis ridged plains region of a few percent for individual ridges and tenths of a percent across whole regions. Plescia (1991) found strain in the Lunae Planum region near Tharsis of ~0.0029 by combining the strain from folding and faulting. These strain results are slightly lower than the strain measured for the wrinkle ridges in NE AD, but within the range of error (Table 7). Thus, the orientation and strain of the wrinkle ridges in this cluster as observed and analyzed in this study are consistent with Tharsis loading.

Northwest Cluster: Not Related to Elysium or Tharsis

The wrinkle ridges in northwestern AD (purple box on Figure 9) are sub-parallel to the edge of Aeolis Planum, and oblique to perpendicular to the highland-lowland dichotomy boundary. They are also marginally closer to the boundary than those in the northeast. Like the wrinkle ridges in the northeast cluster, these northwestern wrinkle ridges are found in an inferred lava substrate (Jacobsen and Burr, 2018). In contrast to

the northeastern cluster, these northwestern wrinkle ridges are more directly south of Elysium Mons and strike in a more N-S direction. If they formed because of stress from Elysium loading, they should have orientations that are concentric to Elysium Mons (Hall et al., 1986). Thus, this orientation of the wrinkle ridges approximately radial to Elysium Mons supports their identification as a distinct group that formed under a different stress field not related to Elysium. However, the N-S orientation of wrinkle ridges here does not match that expected from the modeled compressional stress orientation shown in Figure 10 from Hall et al. (1986), which shows that the largest compressional stress is in the NNW-SSE direction, which would be expected to produce wrinkle ridges in the ENE-WSW direction. The results from the Hall et al. stress map thus indicate that these wrinkle ridges are likely not related to the global stresses from Tharsis either (Figure 20).

The longest ridge in this cluster (#17) appears to overlie Aeolis Serpens, which is thought to be late Hesperian-Amazonian in age (Williams et al., 2013), thus implying that this ridge is younger than Aeolis Serpens (Figure 21). This ridge is contained mostly in the study area, but continues to the north outside of the study area, where this relationship can be seen. However, the other wrinkle ridges in this cluster are found in older lava units which have been buried and exposed (Jacobsen and Burr, 2018). The strain for these wrinkle ridges averages 0.013-0.015 (Table 7). This strain is much higher than the inferred strain from global contraction (0.00011-0.00022; Nahm and Schultz, 2011). Thus, these ridges as observed in this study must have had a more local, but as yet unidentified, source of stress.

East Central Cluster: Evidence for Formation in Sedimentary Rock

The clusters of wrinkle ridges in the northwest and northeast are located in geologic units that are interpreted to be lava plains (Jacobsen and Burr, 2018). The east-central cluster of ridges (yellow box on Figure 9) is located in what may be sedimentary deposits (Kite et al., 2015; Jacobsen and Burr, 2018). In addition, these ridges are all classified as Certain or Probable, indicating a well-formed and/or well-preserved wrinkle ridge morphology. In comparison, the wrinkle ridges in the northeast

and northwest clusters, formed in inferred igneous lava flow lithologies, are classified as Probable with only one Certain example. The results from this study concur with previous studies inferring that wrinkle ridges do not need an underlying igneous lithology to form and can form equally well in sedimentary and igneous lithologies (Plescia and Golombek, 1986; Watters, 1988).

The ridges in the east central cluster are parallel to and near the margin of Zephyria Planum. This location and their N-S orientation are not obviously consistent with loading by Elysium Mons or Tharsis, as was inferred for the northeastern cluster. The orientation of these wrinkle ridges circumferential to the central basin is suggestive of formation in a stress field produced by loading of the central basin, as has been suggested for other basins on the Moon and Mars (Solomon and Head, 1979 and 1980; Thomson and Head, 2001). Such loading could have resulted from the early influx of sediments carried by the inwardly-flowing Noachian rivers (Burr et al., 2016), of which the marginal inverted fluvial deposits (Burr et al., 2009; Kite et al., 2015; Jacobsen and Burr, 2017) are the remnants. This explanation is consistent with the inferred age of the wrinkle ridges in this cluster (Noachian to Hesperian). The thickness of the sediments deposited in AD is estimated to be ~2100m by Kite et al. (2015) in their analysis of the stratigraphy of Aeolis Dorsa. Using this thickness, an average density of sedimentary rocks (2500kg/m^3) and Mars gravity (3.71m/s) as inputs, the horizontal stress caused by loading in AD is $6.49*10^{11}$ Pa. The resulting strain, calculated using an equation relating stress to strain (equation 3.5 from Turcotte and Schubert (2014)), is 0.0000216. This equation uses the stress values, along with values for Young's modulus and Poisson's ratio, to find strain. For this equation I used a Poisson's ratio value of 0.2 as used in this reference for basalt or sandstone and a Young's modulus value of $0.6*10^{11}$ Pa, also for basalt or sandstone. This strain is much less than the strain calculated for any of the wrinkle ridges in this cluster. So while there may have been some influence by stress from loading in AD, it would not have been sufficient to account for the formation of the wrinkle ridges observed in this study and there must have been another as yet unidentified source of stress.

Implications for Stratigraphy

As mentioned in the background, the presence of wrinkle ridges implies layering in the substrate. Large strength contrasts between stratigraphic layers have been suggested as a prerequisite for wrinkle ridge formation by several studies (Plescia and Golombek, 1986; Watters, 1988; Golombek et al., 1991; Mangold et al., 1998; Schultz, 2000). If that suggestion is correct, then the presence of wrinkle ridges in AD as observed in this study implies the presence of one or more weak layers in the stratigraphy there.

Mangold et al. (1998) suggested that wrinkle ridges, especially irregularly shaped or curved ridges, form because of shallow decollements below thrust faults. In the ridged plains region of Mars, these decollements were hypothesized to be due to ice-rich layers interbedded with the widespread lava flows on Mars (Mangold et al. 1998). The presence of ice-rich layers was inferred from fluidized ejecta surrounding craters. Wilson et al. (2018) have inferred the presence of ice within the Western Medusae Fossae Formation (MFF), using a newly reprocessed map of Mars Odyssey Neutron Spectrometer (MONS) data. This map shows the AD region as having a Water Equivalent Hydrogen (WEH) content of >40 wt.%. This result shows too much WEH to be hydrated silicates, implying there is buried water ice or hydrated salts. The stability of hydrated salts on the surface of Mars has not been demonstrated experimentally yet (Bish et al., 2003) although spectral data have led to the inference of salts in recurring slope lineae (Ojha et al., 2015). Although ice is not currently stable at the surface near the equator of Mars, it has been suggested that this ice could be buried by dust layers as with the polar layered deposits (Forget et al., 2006). Thus, buried icy layers are one possibility for layering in the AD region.

Another possibility for layering in the AD region could be the presence of weathered sediment such as clays (Jacobsen and Burr, 2017). Clays can be produced by the weathering of feldspars in igneous rocks (Prothero and Schwab, 2004). These sediments could be interlayered with lava flows, thus providing a weak layer for wrinkle ridge-forming deformation to occur. The presence of cohesive weathered sediments (clays) in southeast AD has been inferred in Jacobsen and Burr (2017) using the

presence of inverted meandering fluvial channels and debris flow deposits on alluvial fans. These cohesive sediments, resulting in meandering fluvial and debris flow deposits, imply that the paleoclimate in this region had a high amount of precipitation and aqueous weathering (Jacobsen and Burr, 2017). While there is no confirmation yet of what constitutes the weak layer in the AD stratigraphy supported by the findings of this study, the previous work discussed here shows that there are several viable options.

Section 6: Conclusions

The small wrinkle ridges in AD identified in this study and the larger ones previously observed and analyzed on the ridged plains of Mars form a size continuum. This continuum suggests they were formed by the same mechanism, in this case, blind thrust faulting, with larger wrinkle ridges having accumulated more strain.

The confined range of geographic orientations of the wrinkle ridges in AD from NW-NE suggests these wrinkle ridges were formed by contraction oriented generally east-west. However, there are several distinct geospatial clusters of wrinkle ridges in AD with distinct orientations and strain values. These distinct orientations and strain values suggest that the different clusters may have had stresses from slightly different causes or acting in different directions. This result supports the alternate hypothesis of this study that contraction in AD was localized throughout the region.

There is evidence for more than one episode of wrinkle ridge formation in Aeolis Dorsa. Based on the location and orientation of the wrinkle ridges in the eastern central cluster relative to the center of AD, these wrinkle ridges may have been influenced by basin loading due to deposition of sediment in the central basin of the Aeolis Dorsa region during the Noachian or Hesperian. However, that explanation only accounts for a small part of the observed strain in this cluster and another source is also needed. The orientation and strain of the wrinkle ridges in the northeast cluster suggest that they formed due to the influence of a stress field related to Tharsis. The wrinkle ridges in this cluster are part of a larger population peripheral to the recent (Amazonian) Cerberus lava flows. Causes of the stress which formed the wrinkle ridges in the northwest and southeast clusters have not yet been identified, although an estimate of the age of the ridges in the northwest cluster is late Hesperian-Amazonian.

Additional findings from this study include evidence of wrinkle ridges formed in sedimentary rocks as well as lava and implications of layered stratigraphy with strength contrasts in Aeolis Dorsa.

The findings from this study show that stress in Aeolis Dorsa was not homogeneous, but instead varied throughout the region and over time.

Future Work

This study has documented the presence and characteristics of small-scale wrinkle ridges along the dichotomy boundary and broadly perpendicular to it. Building on these findings could entail exploring other locations along the dichotomy boundary for additional small-scale wrinkle ridges, as well as modeling the complex stresses in this region to better determine the origin of these small-scale contractional features. Regional mapping and modeling of the large population of NE-SW trending wrinkle ridges near Elysium Mons and the Cerberus plains could also help in constraining a possible source for the regional stress field.

Using the topographic profile data collected for this study, a future study of the directions of vergence, or sense of motion, of the underlying faults could also be conducted. The vergence direction is measured as going towards the steeper side of the ridge. According to Okubo and Schultz (2004), the surface slope of a wrinkle ridge reflects the dip of the underlying fault (Figure 17), thus providing evidence of the direction of fault dip. This work would involve going through each profile to find the fault dip direction and marking how or whether it changes along strike for each wrinkle ridge. These data could then be analyzed using the slope asymmetry method of Okubo and Schultz (2004) to determine the direction of motion. This information would help further constrain the structural history of this area by contributing details of fault directions, thereby suggesting the locations of the driving forces or loads that created the wrinkle ridges.

List of References

Andrews-Hanna, J. C. (2012). The formation of Valles Marineris: 1. Tectonic architecture and the relative roles of extension and subsidence. *Journal of Geophysical Research, 117,* E03006, doi:10.1029/2011JE003953.

Andrews-Hanna, J. C. (2012). The formation of Valles Marineris: 2. Stress focusing along the buried dichotomy boundary. *Journal of Geophysical Research, 117,* E04009, doi:10.1029/2011JE003954.

Bailey, T. C. and Gatrell, A. C. (1995). Interactive Spatial Data Analysis. *Longman Scientific & Technical, Harlow, U.K.* 395 pp.

Berman, D. C., and Hartmann, W. K. (2002). Recent fluvial, volcanic, and tectonic activity on the Cerberus plains of Mars.

Bilotti, F. and Suppe, J. (1999). The global distribution of wrinkle ridges on Venus. *Icarus*, *139*(1), 137-157.

Borden, R. M. and Burr, D. M. (2016). Wrinkle ridges in Aeolis Dorsa, Mars: Preliminary mapping. *Annual Planetary Geologic Mappers Meeting 2016*, abstract #7024.

Borden, R. M., and Burr, D. M. (2017). Investigations of wrinkle ridges in the Aeolis Dorsa region, Mars. *48th Lunar and Planetary Science Conference,* abstract #1056.

Borden, R. M. and Burr, D. M. (2017). Mapping and preliminary analysis of wrinkle ridges in the Aeolis Dorsa region, Mars. *Annual Planetary Geologic Mappers Meeting 2017,* abstract #7056.

Bouley, S., Baratoux, D., Paulien, N., Missenard, Y., and Saint-Bezar, B. (2018). The revised tectonic history of Tharsis. *Earth and Planetary Science Letters, 488,* 126-133, https://doi.org/10.1016/j.epsl.2018.02.019

Boyd, A. S. and Burr, D. M. (2016). Mapping of sand types and dune morphologies in the Aeolis Dorsa region, Western Medusae Fossae Formation, Mars. *Annual Planetary Geologic Mappers Meeting 2016,* abstract #7033.

Boyd, A. S. and Burr, D. M. (2017). Constraining sources of sand in the Aeolis Dorsa region, Mars, via sand dune morphologies and sand distributions. *48th Lunar and Planetary Science Conference,* abstract #1463.

Boyd, A. S. and Burr, D. M. (2018). Investigating the sources and origins of dark sand in Aeolis Dorsa, Mars: Evidence for dark sand production. *49th Lunar and Planetary Science Conference,* abstract #2734.

Brandes, C., & Tanner, D. C. (2014). Fault-related folding: A review of kinematic models and their application. *Earth-Science Reviews*, *138*, 352–370. http://doi.org/10.1016/j.earscirev.2014.06.008

Burr, D. M., Enga, M. T., Williams, R. M., Zimbelman, J. R., Howard, A. D., & Brennand, T. A. (2009). Pervasive aqueous paleoflow features in the Aeolis/Zephyria Plana region, Mars. *Icarus*, *200*(1), 52-76.

Burr, D. M., Zimbelman, J. R., Qualls, F. B., Chojnacki, M., Murchie, S. L., and Michaels, T. I. (2011). The western Medusae Fossae formation, Mars: A possible source of dark aeolian sand. *42nd Lunar and Planetary Science Conference,* abstract #1582.

Burr, D. M., de Silva, S. L., Zimbelman, J. R., and Bridges, N. T. (2012). Aeolian dunes from volcaniclastic sediments: The Medusae Fossae formation, Mars, and Andean ignimbrites, Earth. *43rd Lunar and Planetary Science Conference,* abstract #1692.

Burr, D. M., Jacobsen, R. E., Lefort, A., Borden R. M., and Boyd, A. S. (2016).

Continuing to characterize the history of a diverse inverted landscape: Mapping of the Aeolis Dorsa region, Mars. *Annual Planetary Geologic Mappers Meeting,* abstract #7013.

Burr, D. M., Jacobsen, R. E., Lefort, A., Borden, R. M., Boyd, A. S., and Peel, S. E. (2017). Update on mapping of the Aeolis Dorsa region, Mars: Finding ever more diversity in this inverted landscape. *Annual Planetary Geologic Mappers Meeting,* abstract #7010.

Byrne, P. K., Klimczak, C., Celâl Şengör, a. M., Solomon, S. C., Watters, T. R., Hauck II, S. a., & Şengör, a. M. C. (2014). Mercury's global contraction much greater than earlier estimates. *Nature Geoscience*, *7*(4), 301–307. http://doi.org/10.1038/ngeo2097

Casale, G. and Pratt, T. L. (2015). Thin-or Thick-Skinned Faulting in the Yakima Fold and Thrust Belt (WA)? Constraints from Kinematic Modeling of the Saddle Mountains Anticline. *Bulletin of the Seismological Society of America, 105,* 745-752. http://doi.org/10.1785/0120140050

Chicarro, A. F., Schultz, P. H., and Masson, P. (1985). Global and regional ridge patterns on Mars. *Icarus, 63,* 153-174.

Christensen, P. R., Jakosky, B. M., Kieffer, H. H., Malin, M. C., McSween, H. Y., Nealson, Jr. K., Mehall, G. L., Silverman, S. H., Ferry, S., Caplinger, M., and Ravine M. (2004). The Thermal Emission Imaging System (THEMIS) for the Mars 2001 Odyssey mission, *Space Sci. Rev., 110*, 85-130.

Cunje, A. B. and Ghent, R. R. (2016). Caloris basin, Mercury: History of deformation from an analysis of tectonic landforms. *Icarus, 268,* 131-144, http://dx.doi.org/10.1016/j.icarus.2015.12.033

Davis, P. A., & Golombek, M. P. (1990). Discontinuities in the shallow Martian crust at Lunae, Syria, and Sinai Plana. *Journal of Geophysical Research: Solid Earth, 95*(B9), 14231-14248.

Fassett, C. I. (2016). Ames stereo pipeline-derived digital terrain models of Mercury from MESSENGER stereo imaging. *Planetary and Space Science, 134,* 19-28.

Fossen, H. (2010). *Structural geology.* New York, NY: Cambridge University Press.

Golombek, M. P., Plescia, J. B., and Franklin, B. J. (1991). Faulting and folding in the formation of planetary wrinkle ridges. *Proceedings of Lunar and Planetary Science, 21*, 679-693.

Golombek, M. P., Anderson, F. S., and Zuber, M. T. (2001). Martian wrinkle ridge topography: Evidence for subsurface faults from MOLA. *Journal of Geophysical Research E: Planets*, *106*(E10), 23811–23821.

Golombek, M. P. and Phillips, R. J. (2010). Mars Tectonics. In *Planetary Tectonics* (pp. 183–232).

Irwin, R. P. III and Watters, T. R. (2010). Geology of the Martian crustal dichotomy boundary: Age, modifications, and implications for modeling efforts. *Journal of Geophysical Research, 115,* E11006, doi:10.1029/2010JE003658

Irwin, R. P., III, T. R. Watters, A. D. Howard, and J. R. Zimbelman. (2004). Sedimentary resurfacing and fretted terrain development along the crustal dichotomy boundary, Aeolis Mensae, Mars. *JGR,* 109, E09011. doi:10.1029/2004JE002248.

Jacobsen, R.E., and Burr, D.M. (2017). Dichotomies in the fluvial and alluvial fan deposits of the Aeolis Dorsa, Mars: Implications for weathered sediment and paleoclimate. *Geosphere, v. 13*, no. 6. doi:10.1130/GES01330.1

Jacobsen, R. E., and Burr, D. M. (2018). Synthesizing the history of a diverse inverted landscape: Mapping of the Aeolis Dorsa region, Mars. *49th Lunar and Planetary Science Conference,* Abstract #2057

Jacobsen, R. E., Burr, D. M., Peel, S. E., Borden, R. M., and Boyd, A. S. (2018). Understanding the history of a diverse inverted landscape: Summary and plan for finishing the 1: 500k geologic map of Aeolis Dorsa, Mars. *Annual Planetary Geologic Mappers Meeting*, Abstract #7014

Jaeger, W. L., Keszthelyi, L. P., Skinner, J. A., Milazzo, M. P., McEwen, A. S., Titus, T. N., Rosiek, M.R., Galuszka, D.M., Howington-Kraus, E., Kirk, R. L., the HiRISE Team. (2010). Emplacement of the youngest flood lava on Mars: A short, turbulent story. *Icarus, 205(1),* 230-243.

Kerber, L. and Head, J. W. (2010). The age of the Medusae Fossae Formation: Evidence for Hesperian emplacement from crater morphology, stratigraphy, and ancient lava contacts. *Icarus, 206,* 669-684. doi:10.1016/j.icarus.2009.10.001

Keszthelyi, L., McEwen, A. S., and Thordarson, T. (2000). Terrestrial analogs and thermal models for Martian flood lavas. *Journal of Geophysical Research: Planets (1991–2012), 105(E6),* 15027-15049.

Keszthelyi, L., Thordarson, T., McEwen, A., Haack, H., Guilbaud, M. N., Self, S., and Rossi, M. J. (2004). Icelandic analogs to Martian flood lavas. *Geochemistry, Geophysics, Geosystems, 5(11).*

Kite, E. S., Howard, A. D., Lucas, A. S., Armstrong, J. C., Aharonson, O., and Lamb, M. P. (2015). Stratigraphy of Aeolis Dorsa, Mars: Stratigraphic context of the great river deposits. *Icarus*, *253*, 223–242. http://doi.org/10.1016/j.icarus.2015.03.007

Klimczak, C., Watters, T. R., Ernst, C. M., Freed, A. M., Byrne, P. K., Solomon, S. C., Blair, D. M., and Head, J. W. (2012). Deformation associated with ghost craters and basins in volcanic smooth plains on Mercury: Strain analysis and implications for plains evolution. *J. Geophys. Res., 117,* E00L03, doi:10.1029/2012JE004100.

Lefort, A., Burr, D. M., Beyer, R. A., and Howard, A. D. (2012). Inverted fluvial features in the Aeolis-Zephyria Plana, western Medusae Fossae Formation, Mars: Evidence for post-formation modification. *Journal of Geophysical Research, 117,* E03007, doi:10.1029/2011JE004008

Lefort, A., Burr, D. M., Nimmo, F., and Jacobsen, R. E. (2015). Channel slope reversal near the Martian dichotomy boundary: Testing tectonic hypotheses. *Geomorphology*, *240*, 121–136. http://doi.org/10.1016/j.geomorph.2014.09.028

Li, B., Ling, Z., Zhang, J., Chen, J., Ni, Y., and Liu, C. (2018). Displacement-length ratios and contractional strains of lunar wrinkle ridges in Mare Serenitatis and Mare Tranquillitatis. *Journal of Structural Geology, 109,* 27-37, https://doi.org/10.1016/j.jsg.2018.01.003

Lucchitta, B. K. (1977). Topography, structure, and mare ridges in southern Mare Imbrium and northern Oceanus Procellarum. *Proceedings of the Lunar Science Conference*, 2691–2703.

Malin, M. C., Bell, J. F. III, Cantor, B. A., Caplinger, M. A., Calvin, W. M., Clancy, R. T., Edgett, K. S., Edwards, L., Haberle, R. M., James, P. B., Lee, S. W., Ravine, M.

A., Thomas, P. C., and Wolff, M. J. (2007). Context Camera investigation on board the Mars Reconnaissance Orbiter. *Journal of Geophysical Research, 112,* E05S04, doi:10.1029/2006JE002808

Mandt, K. E., de Silva, S. L., J. R. Zimbelman, and D. A. Crown. (2008). Origin of the Medusae Fossae Formation, Mars: Insights from a synoptic approach. *JGR*, 113, E12011, doi:10.1029/2008JE003076.

Mangold, N., Allemand, P., and Thomas, P. G. (1998). Wrinkle ridges of Mars: structural analysis and evidence for shallow deformation controlled by ice-rich décollements. *Planetary and Space Science*, *46*(4), 345–356. http://doi.org/10.1016/s0032-0633(97)00195-5

Montési, L. and Zuber, M. T. (2003). Clues to the lithospheric structure of Mars from wrinkle ridge sets and localization instability. *Journal of Geophysical Research*, *108*(E6), 5048. http://doi.org/10.1029/2002JE001974

Moratto, Z. M., M. J. Broxton, R. A. Beyer, M. Lundy, and K. Husmann. (2010). Ames Stereo Pipeline, NASA's Open Source Automated Stereogrammetry Software. Lunar and Planetary Science Conference 41, abstract #2364.

Mueller, K. and Golombek, M. (2004). Compressional Structures on Mars. *Annual Review of Earth and Planetary Sciences*, *32*(1), 435–464. http://doi.org/10.1146/annurev.earth.32.101802.120553

Nimmo, F. (2005). Tectonic consequences of Martian dichotomy modification by lower-crustal flow and erosion. *Geology*, *33*(7), 533–536. doi: 10.1130/G21342.1

Ojha, L., Lewis, K., and Karunatillake, S. (2017). The density of the Medusae Fossae Formation: Implications for its composition, origin, and importance in Martian

history. *Geological Society of America Abstracts with Programs, vol. 49,* no 6. doi: 10.1130/abs/2017AM-297627

Okubo, C. H. and Schultz, R. A. (2004). Mechanical stratigraphy in the western equatorial region of Mars based on thrust fault-related fold topography and implications for near-surface volatile reservoirs. *Bulletin of the Geological Society of America*, *116*(5-6), 594–605. http://doi.org/10.1130/B25361.1

Pain, C. F., Clarke, J. D. A., and Thomas, M. (2007). Inversion of relief on Mars. *Icarus, 190,* 478-491, doi:10.1016/j.icarus.2007.03.017

Peel, S. E. and Burr, D. M. (2018). Intracrater deposits in the Aeolis Dorsa Region, Mars: Evidence for Lakes? *Lunar and Planetary Science Conference, 49,* Abstract #1006.

Plescia, J. B. (1986). Tectonics of the Elysium region, Mars. *Lunar and Planetary Science XVII,* 672-673.

Plescia, J. B. (1991). Wrinkle ridges in Lunae Planum, Mars: Implications for shortening and strain. *Geophysical Research Letters, 18,* 913-916.

Plescia, J. B. and Golombek, M. P. (1986). Origin of planetary wrinkle ridges based on the study of terrestrial analogs. *Geological Society of America Bulletin*, *97*(11), 1289–1299. http://doi.org/10.1130/0016-7606(1986)97<1289:OOPWRB>2.0.CO

Prothero, D. R., and Schwab, F. (2004). *Sedimentary geology*. Macmillan.

Reidel, S. P. (1984). The Saddle Mountains: The evolution of an anticline in the Yakima Fold Belt. *American Journal of Science, 284,* 942-978.

Reidel, S. P., Tolan, T. L., Hooper, P. R., Beeson, M. H., Fecht, K. R., Bentley, R. D. and Anderson, J. L. (1989). The Grande Ronde Basalt, Columbia River Basalt Group; Stratigraphic descriptions and correlations in Washington, Oregon, and Idaho. *Volcanism and tectonism in the Columbia River flood-basalt province: Geological Society of America Special Paper*, *239*, 21-53.

Schultz, R. A. (2000). Localization of bedding plane slip and backthrust faults above blind thrust faults: Keys to wrinkle ridge structure. *Journal of Geophysical Research*, *105*(E5), 12035. http://doi.org/10.1029/1999JE001212

Scott, D. H. and Tanaka, K. L. (1982). Ignimbrites of Amazonis Planitia region of Mars. *Journal of Geophysical Research, 87,* 1179-1190, doi:10.1029/JB087iB02p01179

Scott, D. H. and Tanaka, K. L. (1986). The youngest channel system on Mars. *Lunar and Planetary Science XVII,* 856-866.

Sharpton, V. L. and Head, J. W. III. (1988). Lunar mare ridges: Analysis of ridge-crater intersections and implications for the tectonic origin of mare ridges. *Lunar and Planetary Science Conference Proceedings XVIII,* 307-317.

Silverman, B. W. (1986). *Density Estimation for Statistics and Data Analysis*. New York, New York: Chapman and Hall.

Smart, K. J., Ferrill, D. A., & Colton, S. L. (2006). En Échelon Segmentation of Wrinkle Ridges in Solis Planum, Mars, and Implications for Counter-Clockwise Rotation of Shortening Direction. *Lunar and Planetary Science Conference*, *37*, 1–2.

Smith, D. E., Zuber, M. T., Frey, H. V., Garvin, J. B., Head, J. W., Muhleman, D. O., Pettengill, G. H., Phillips, R. J., Solomon, S. C., Zwally, H. J., Banerdt, W. B., Duxbury, T. C., Golombek, M. P., Lemoine, F. G., Neumann, G. A., Rowlands, D. D., Aharonson, O., Ford, P. G., Ivanov, A. B., Johnson, C. L., McGovern, P. J.,

Abshire, J. B., Afzal, R. S., and Sun, X. (2001). Mars Orbiter Laser Altimeter: Experiment summary after the first year of global mapping of Mars. *Journal of Geophysical Research, 106,* 23689-23722, https://doi.org/10.1029/2000JE001364

Solomon, S. C. and Head, J. W. (1979). Vertical movement in mare basins: Relation to mare emplacement, basin tectonics, and lunar thermal history. *Journal of Geophysical Research, v. 84,* p. 1667-1682, doi:10.1029/JB084iB04p01667

Solomon, S. C. and Head, J. W. (1980). Lunar mascon basins: Lava filling, tectonics, and evolution of the lithosphere. *Reviews of Geophysics and Space Physics, v. 18,* p. 107-141, doi: 10.1029/RG018i001p00107

Solomon, S.C., McNutt, R.L., Jr., Watters, T.R., Lawrence, D.J., Feldman, W.C., Head, J.W., Krimigis, S.M., Murchie, S.L., Phillips, R.J., Slavin, J.A., and Zuber, M.T. (2008). Return to Mercury: A global perspective on MESSENGER's first Mercury flyby. *Science, v. 321,* p. 59–62, doi:10.1126/science.1159706.

Strom, R.G., Trask, N.J., and Guest, J.E. (1975). Tectonism and volcanism on Mercury. *Journal of Geophysical Research, v. 80,* p. 2478–2507, doi:10.1029 /JB080i017p02478.

Tanaka, K. L. (2000). Dust and ice deposition in the Martian geologic record. *Icarus, 144,* 254-266, https://doi.org/10.1006/icar.1999.6297

Tanaka, K. L. and Golombek, M P. (1989). Martian tension fractures and the formation of grabens and collapse features at Valles Marineris. *Lunar and Planetary Science Conference Proceedings XIX,* 383-396.

Tanaka, K. L. Skinner, J. A., Jr., Hare, T. M., Joyal, T., and Wenker, A. (2003). Resurfacing history of the northern plains of Mars based on geologic mapping of Mars Global Surveyor data. *Journal of Geophysical Research, 108*(E4)*,* 8043,

doi:10.1029/2002JE001908

Tanaka, K.L., Skinner, J.A., Jr., Dohm, J.M., Irwin, R.P., III, Kolb, E.J., Fortezzo, C.M., Platz, T., Michael, G.G., and Hare, T.M. (2014). Geologic map of Mars: U.S. Geological Survey Scientific Investigations Map 3292, scale 1:20,000,000, pamphlet 43 p., *http://dx.doi.org/10.3133/sim3292*.

Thomson, B. J. and Head, J. W. (2001). Utopia Basin, Mars: Characterization of topography and morphology and assessment of the origin and evolution of basin internal structure. *Journal of Geophysical Research: Planets, 106(E10),* 23209-23230, https://doi.org/10.1029/2000JE001355

Vaucher, J., Baratoux, D., et al. (2009). The volcanic history of central Elysium Planitia: Implications for martian magmatism. Icarus, 204(2), 418-442.

Ward, A. W. (1979). Yardangs on Mars: Evidence of recent wind erosion. *Journal of Geophysical Research, 84(B14)*, 8147–8166. doi:10.1029/JB084iB14p08147.

Watters, T. R. (1988). Wrinkle Ridge Assemblages on the Terrestrial Planets. *Journal of Geophysical Research*, *93*(B9), 10236–10254.

Watters, T. R. (1989). Periodically spaced anticlines of the Columbia Plateau. From *Geological Society of America Special Paper 239.* http://doi.org/10.1130/SPE239-p283

Watters, T. R. (1991). Origin of periodically spaced wrinkle ridges on the Tharsis plateau of Mars. *Journal of Geophysical Research, 96,* 15599-15616, https://doi.org/10.1029/91JE01402

Watters, T. R. (1993). Compressional tectonism on Mars. *Journal of Geophysical*

Research, 98, 17049-17060, https://doi.org/10.1029/93JE01138

Watters, T. R. (2003). Lithospheric pressure and the origin of the dichotomy boundary on Mars. *Geology, 31,* 271-274, https://doi.org/10.1130/0091-7613(2003)031<0271:LFATOO>2.0.CO;2

Watters, T. R. (2003). Thrust faults along the dichotomy boundary in the eastern hemisphere of Mars. *Journal of Geophysical Research Planets, 108,* 5054, DOI 10.1029/2002JE001934

Watters, T. R. and Robinson, M. S. (1997). Radar and photoclinometric studies of wrinkle ridges on Mars. *Journal of Geophysical Research, 102,* 10889-10904, https://doi.org/10.1029/97JE00411

Watters, T. R. and Robinson, M. S. (1999). Lobate scarps and the Martian crustal dichotomy. *Journal of Geophysical Research, 104,* 18981-18990, https://doi.org/10.1029/1998JE001007

Watters, T. R., Murchie, S. L., Robinson, M. S., Solomon, S. C., Denevi, B. W., Andre, S. L., and Head. J. W. (2009). Emplacement and tectonic deformation of smooth plains in the Caloris basin, Mercury. *Earth and Planetary Science Letters, 285,* 309-319, https://doi.org/10.1016/j.epsl.2009.03.040

Watters, T. R. and Schultz, R. A. (2010). *Planetary Tectonics*. New York: Cambridge University Press.

Wells, G. L. and Zimbelman, J. R. (1997). Extraterrestrial arid surface processes. *Arid Zone Geomorphology: Process, Form, and Change in Drylands, pp 659-690.*

Williams, R. M. E., Irwin, R. P., Burr, D. M., Harrison, T., and McClelland, P. Variability

in martian sinuous ridge form: Case study of Aeolis Serpens in the Aeolis Dorsa, Mars, and insight from the Mirackina paleoriver, South Australia. *Icarus, 225,* 308-324, https://doi.org/10.1016/j.icarus.2013.03.016

Wilson, J. T., Eke, V. R., Massey, R. J., Elphic, R. C., Feldman, W. C., Maurice, S., & Teodoro, L. F. (2018). Equatorial locations of water on Mars: Improved resolution maps based on Mars Odyssey Neutron Spectrometer data. *Icarus*, *299*, 148-160.

Yong Technology Inc. (2014). GeoRose. Edmonton, Canada. http://www.yongtechnology.com/download/georose

Yue, Z., Li, W., Di, K., Liu, Z., and Liu, J. (2015). Global mapping and analysis of lunar wrinkle ridges. *Journal of Geophysical Research: Planets, 120,* 978-994. doi:10.1002/2014JE004777

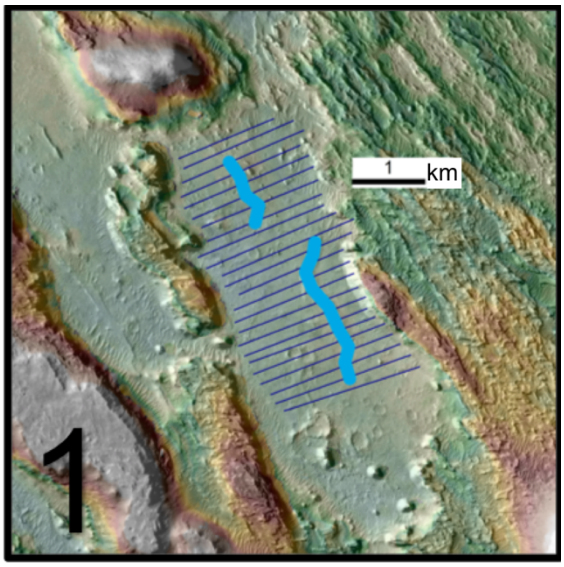
Appendix

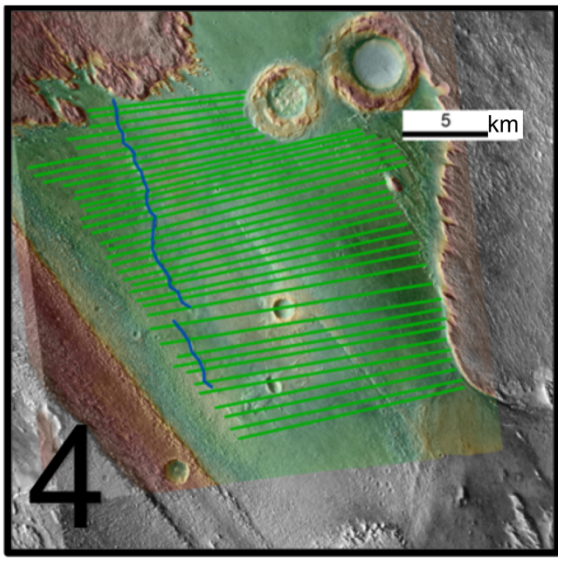
Steps for DEM Image Processing

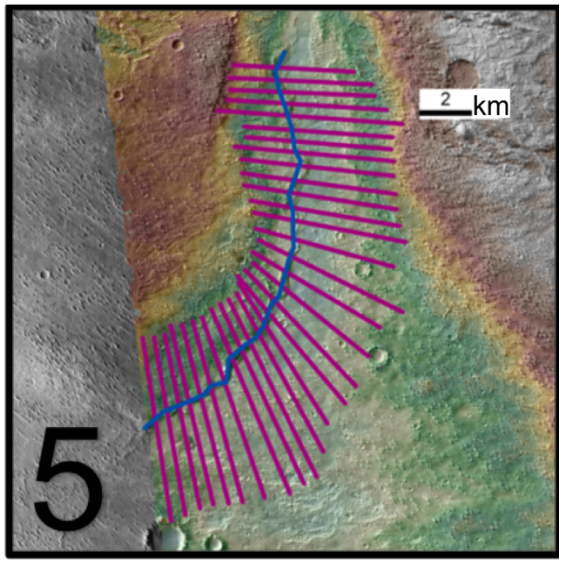
The following steps were used in the Imaging Software for Imagers and Spectrometers 3 (ISIS3) program to process CTX stereo pair images before merging into a DEM. First, the images were downloaded as .IMG files using the Planetary Image Locator Tool (PILOT; https://pilot.wr.usgs.gov/). Using ISIS3, the images were converted from .IMG to .cub files using the “mroctx2isis” command. Latitude and longitude information, along with other information collectively called SPICE, is added using the “spiceinit” command. The images are then radiometrically corrected using the “ctxcal” command. Both images are opened in a program called qview and the higher resolution image is visually determined. The images are then map projected using the “cam2map” command, with the lower resolution image projected first and the second image matched to it.

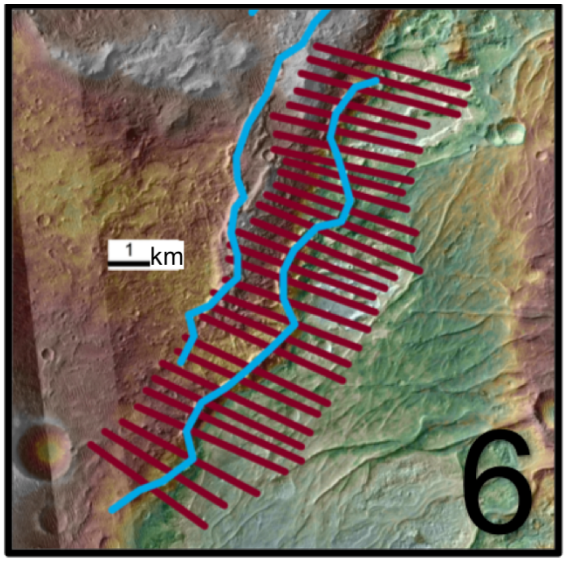
The following steps and settings were used in the Ames Stereo Pipeline Software to create DEMs from stereo pairs. First, a stereo.txt file was made specifically for this project, with the cost-function mode set to 0 (absolute difference) rather than 2 (normalized cross correlation). This file was used for the stereo command, for which the higher resolution image is listed first. The “caminfo” command was used on the lower resolution image. This information is used to find the center latitude and longitude for the final step. This step is completed using the “point2dem” command and the PC.tif file which resulted from the stereo command. The flags added to this command are the following: -r mars --sinusoidal --proj-lon *center longitude to two decimal places* --dem-spacing 15. -r indicates the body the images are from. Sinusoidal is the map projection to be used. DEM spacing refers to the output resolution of the DEM file.

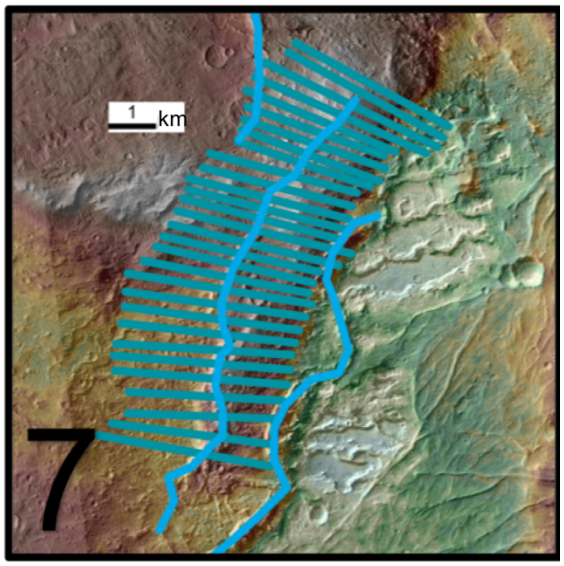
Below are shown the 12 wrinkle ridges for which DEMs were created, along with the topographic profile lines drawn in ArcMap.

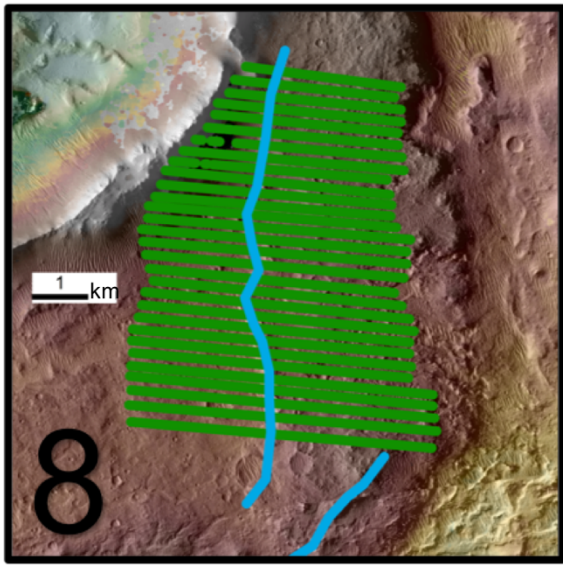

1 km
1

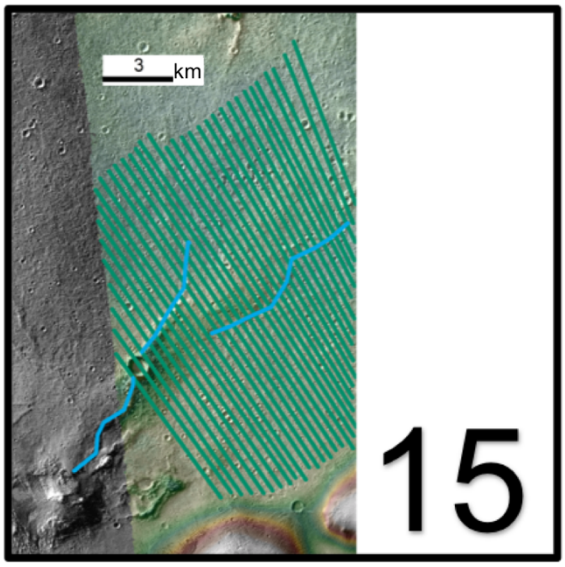

5 km
4

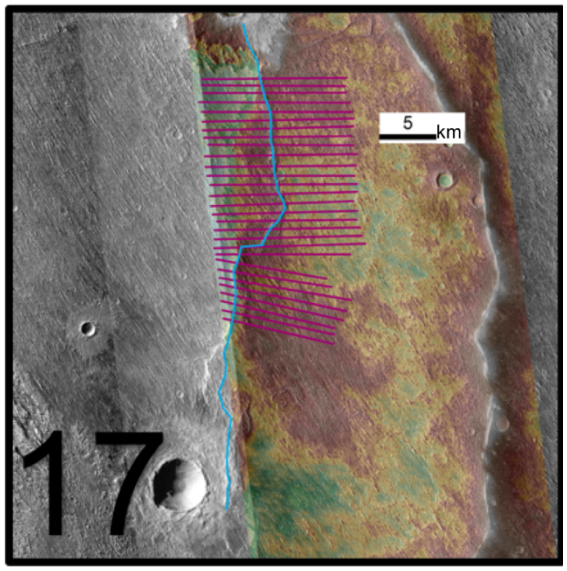

2 km
5

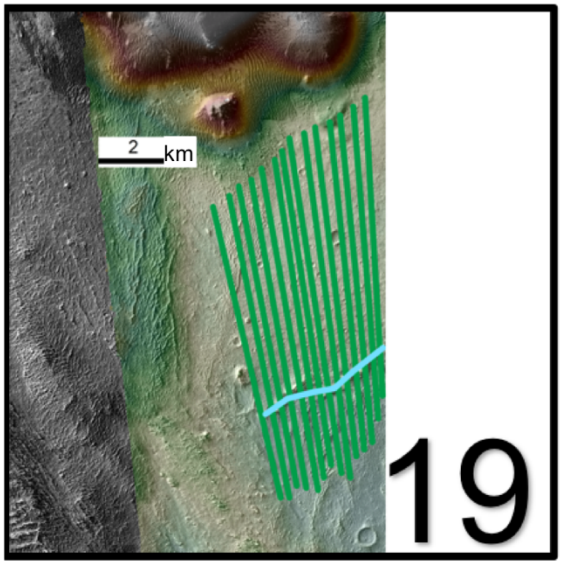

1 km
6

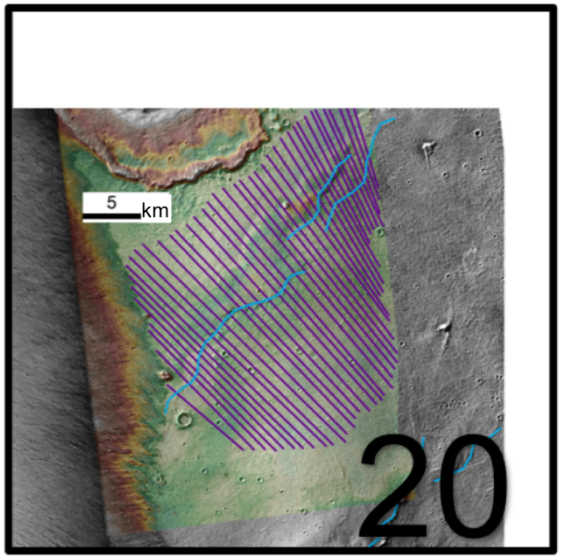

1 km
7

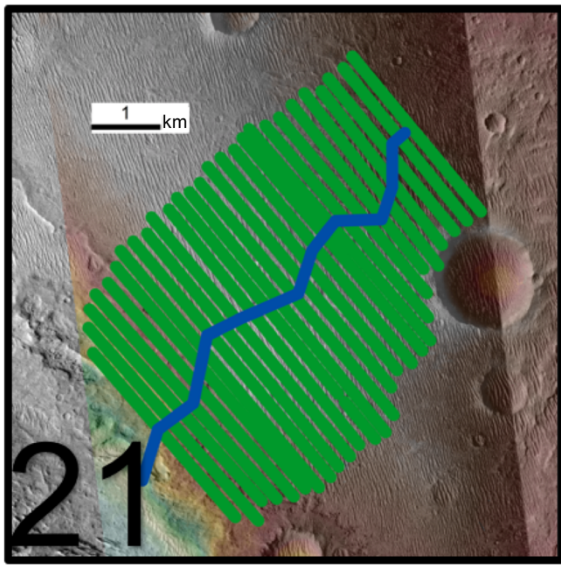

1 km
8

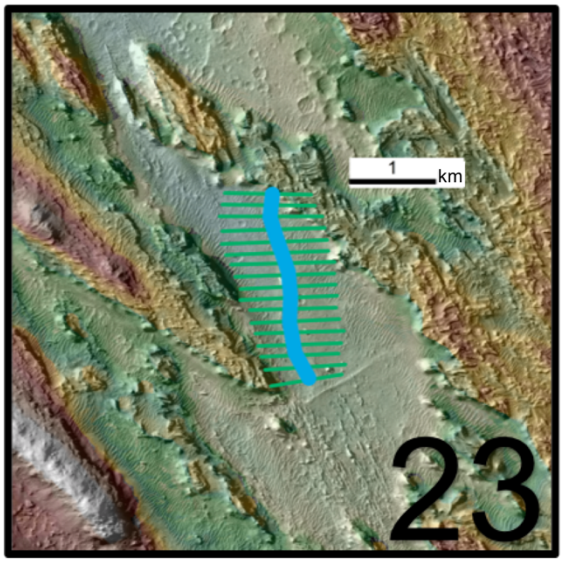

3 km
15


5 km
17


2 km
19


5 km
20


1
km
21


1
km
23

Figures and Tables

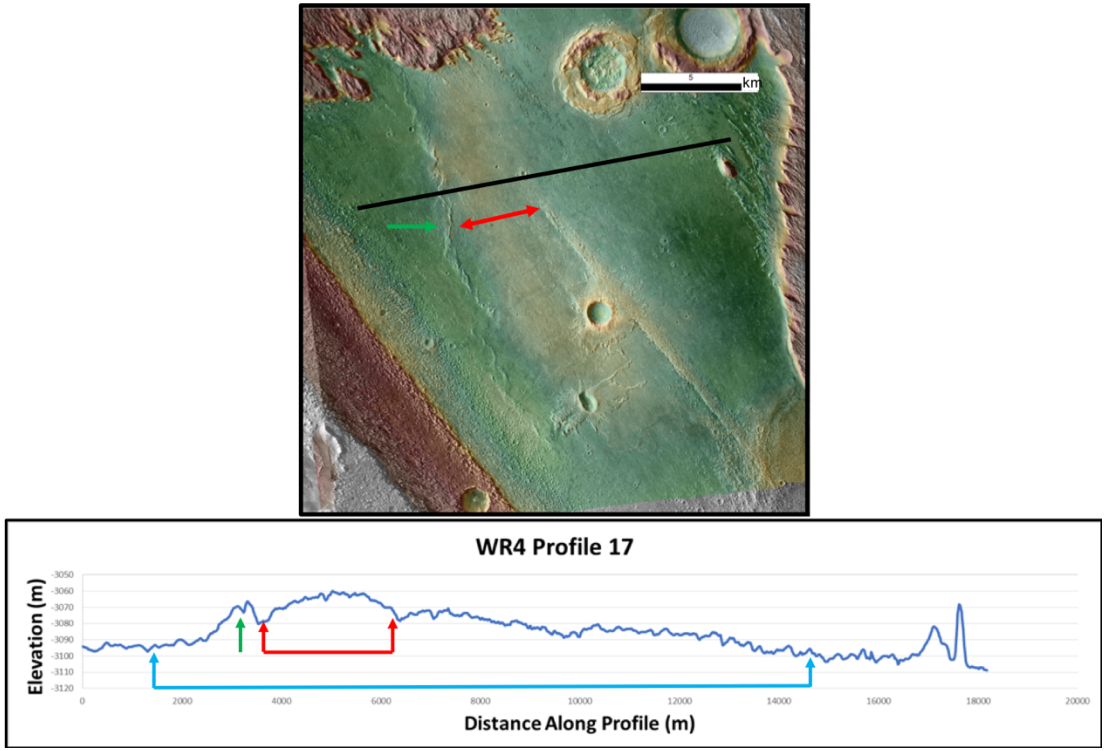


Figure 1: Top: CTX DEM covering wrinkle ridge #4 in AD (for location, see Figure 5). The black line shows the location of the profile in the bottom image. The narrow crenulated ridge can be easily seen running NW-SE on the western side of the image and is pointed out by the red arrow. The broad arch is covered by the green double-sided arrow. Warm colors are high elevations and cool colors are low elevations. Scale bar is 5 km. Bottom: Topographic profile of wrinkle ridge #4. The blue arrow shows the low topographic rise, the red arrow shows the broad arch or hill, and the green arrow shows the narrow crenulation at crest.

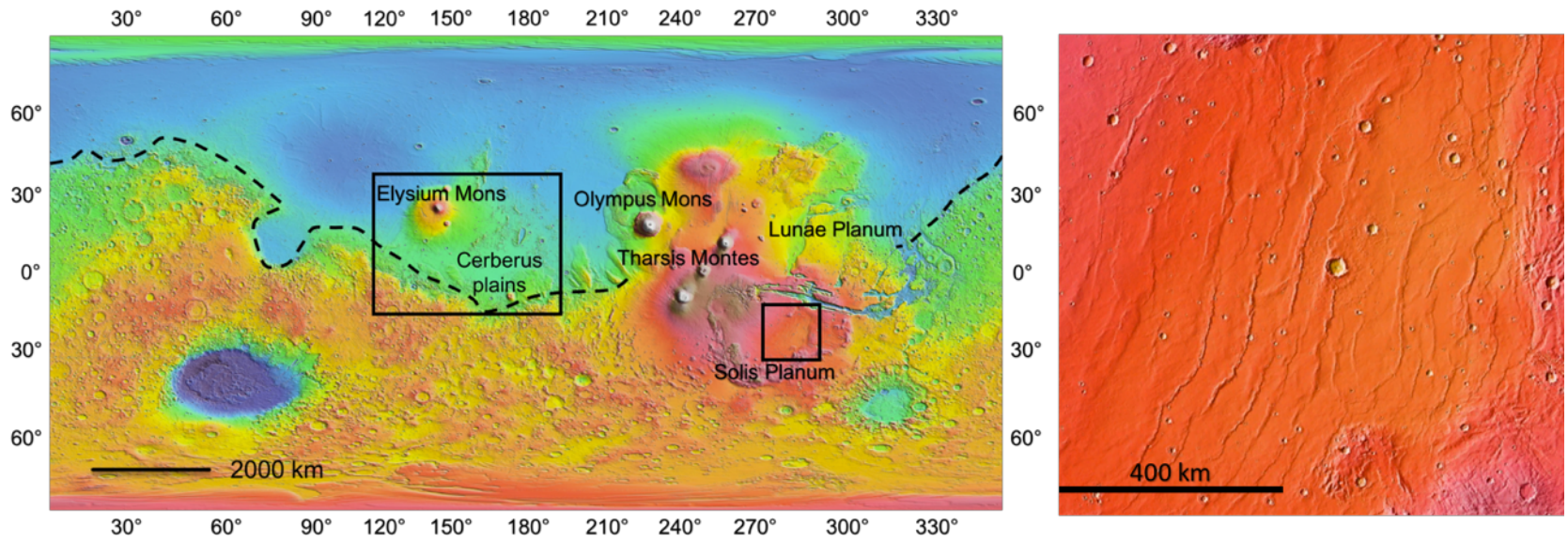


Figure 2: (Left) Global map of Mars with colorized Mars Orbiter Laser Altimeter (MOLA) elevations, where warm colors are high and cool colors are low. Dashed line approximates the global dichotomy boundary. Black box with Elysium Mons and Cerberus Plains shows area of Figure 4. Black box around Solis Planum shows location of image at right. (Right) Large wrinkle ridges on Solis Planum.

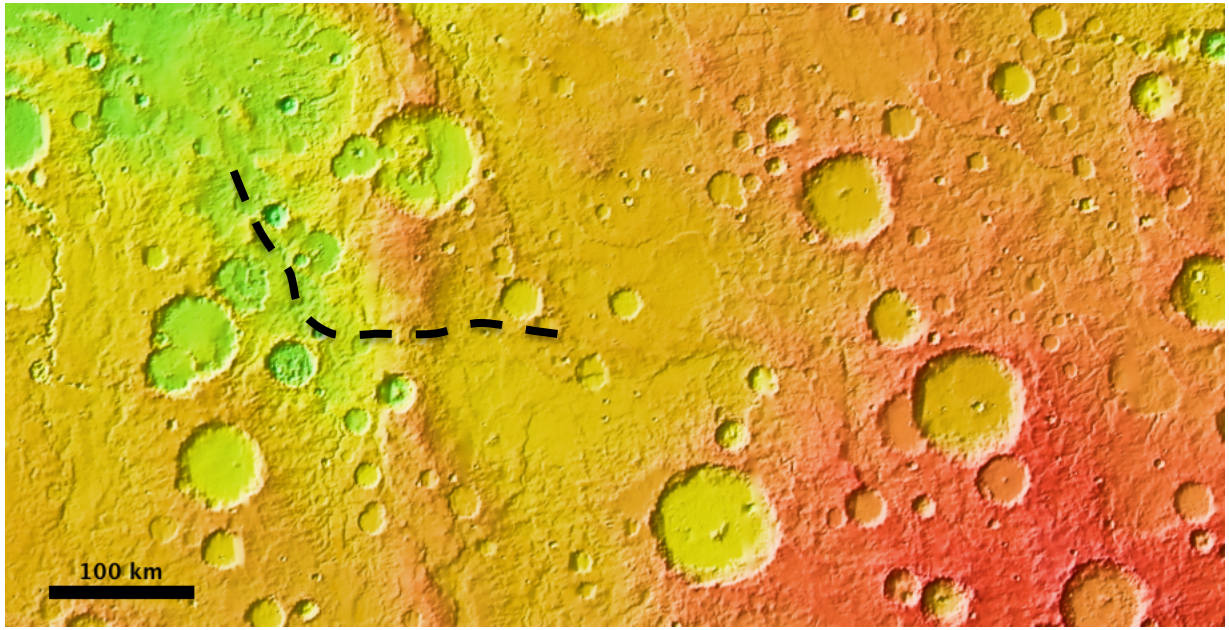


Figure 3: Lobate scarp (indicated by dashed black line) in the southern highlands, located at approximately 117° E and 5° S.

Table 1: Geologic settings and hypothesized formation mechanisms for wrinkle ridges on various planetary bodies.

Planetary Body	**Location(s) of wrinkle ridges**	**Hypothesized cause (mechanism) of formation**	**Reference(s)**
Mercury	Smooth plains and cratered plains	Contraction from planetary cooling	Strom et al., 1975; Watters, 1988; Watters et al., 2009; Byrne et al., 2014
Venus	Ridged volcanic plains in lowlands	Slip on thrust faults caused by compressive lithospheric thermal stresses induced by surface temperature increase	Watters, 1988; Bilotti and Suppe, 1999; Dragoni and Piombo, 2003
Earth	Foreland basins related to subduction zones; fold-and-thrust belts; thrust fault scarps	Folding of surface rocks over thrust faults at depth in compressional regimes with mechanically contrasting layers	Plescia and Golombek, 1986; Watters, 1988 and 1989
Moon	Maria basalts, some extend to highlands	Subsidence of Mare deposits as they cooled	Maxwell et al., 1975; Solomon and Head, 1980; Watters, 1988; Yue et al., 2015; Li et al., 2018
Mars	Smooth plains, filled craters, shield volcano calderas, highland plains areas	Surface folding above blind thrust faults in lithologies with layering/mechanical strength contrasts	Chicarro et al., 1985; Watters, 1988; Mangold et al., 1997; Watters and Robinson, 1997; Schultz, 2000; Golombek et al., 2001; Mueller and Golombek, 2004; Golombek and Phillips, 2010

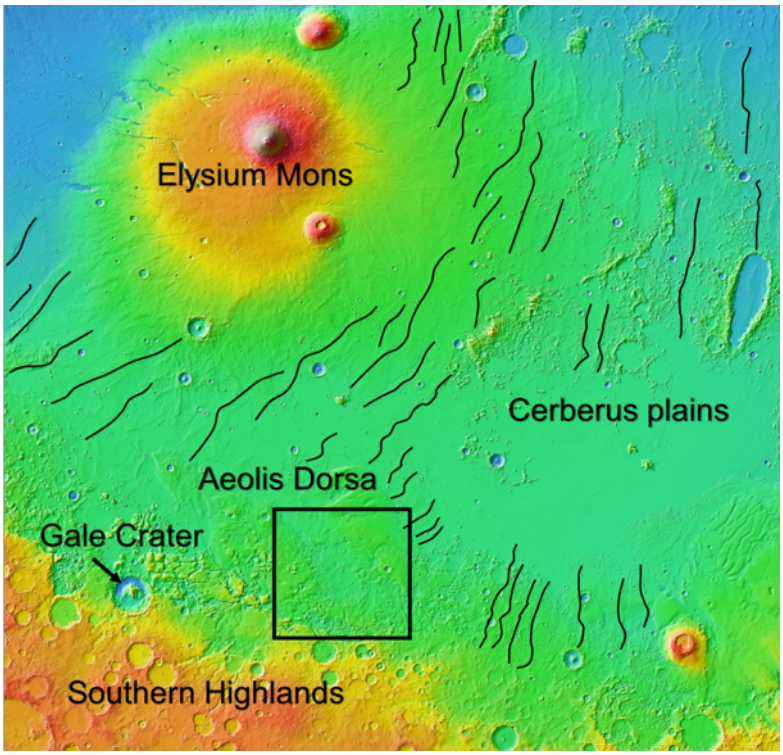


Figure 4: Regional image of Elysium Mons and the Aeolis Dorsa region. Black lines show approximate locations of a sampling of wrinkle ridges near Elysium Mons. Black box shows location of Aeolis Dorsa study area (Figure 6).

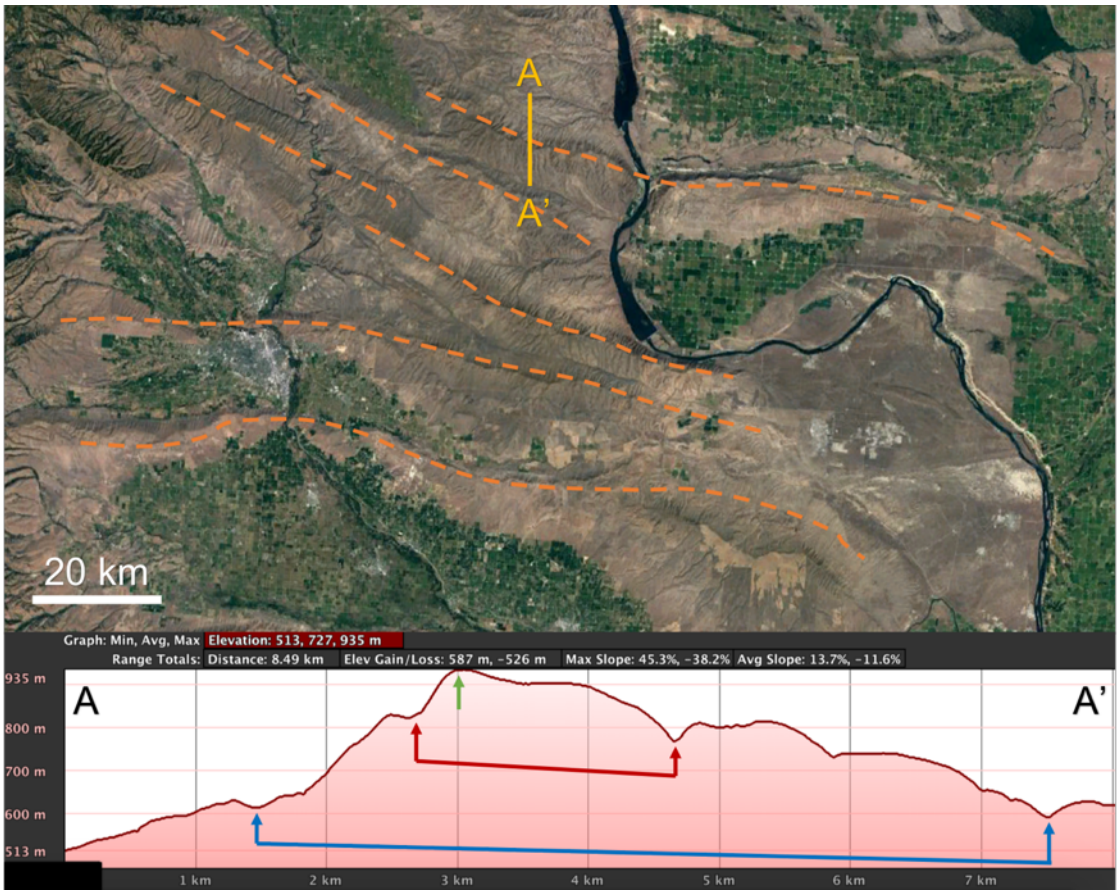


Figure 5: Top: Image from Google Earth of several ridges in the Yakima Fold and Thrust Belt of central Washington state, a proposed terrestrial analog for wrinkle ridges on other planets (Reidel, 1984; Watters, 1988). Orange dashed lines show approximate trace of ridge crests. Bottom: Elevation profile of the Saddle Mountain anticline with topography taken from Shuttle Radar Topography Mission data is from A to A' (shown on top image). Colored arrows indicate the three morphologic parts of a wrinkle ridge: Blue arrows indicate edges of topographic rise, red arrows indicate broad arch or hill, green arrow indicates narrow crenulation at crest.

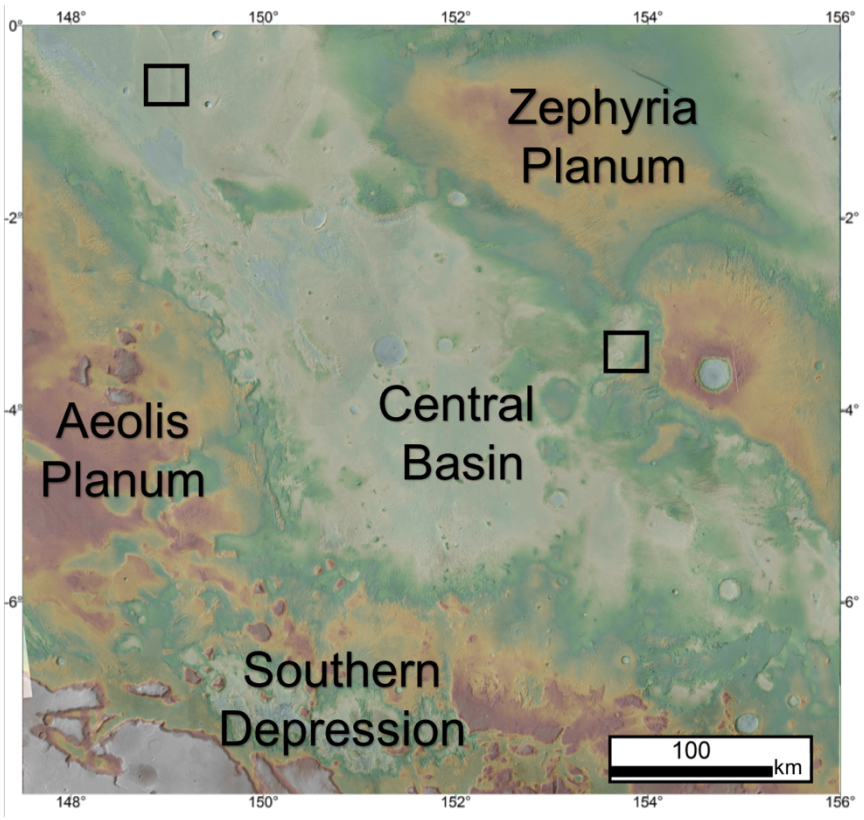


Figure 6: CTX mosaic basemap of Aeolis Dorsa study area with colorized MOLA elevations, where warm colors are high and cool colors are low. Aeolis and Zephyria Plana are mapped as part of the Medusae Fossae Formation (MFF), a hypothesized ignimbrite or pyroclastic deposit. Black boxes show locations of images in Figure 8.

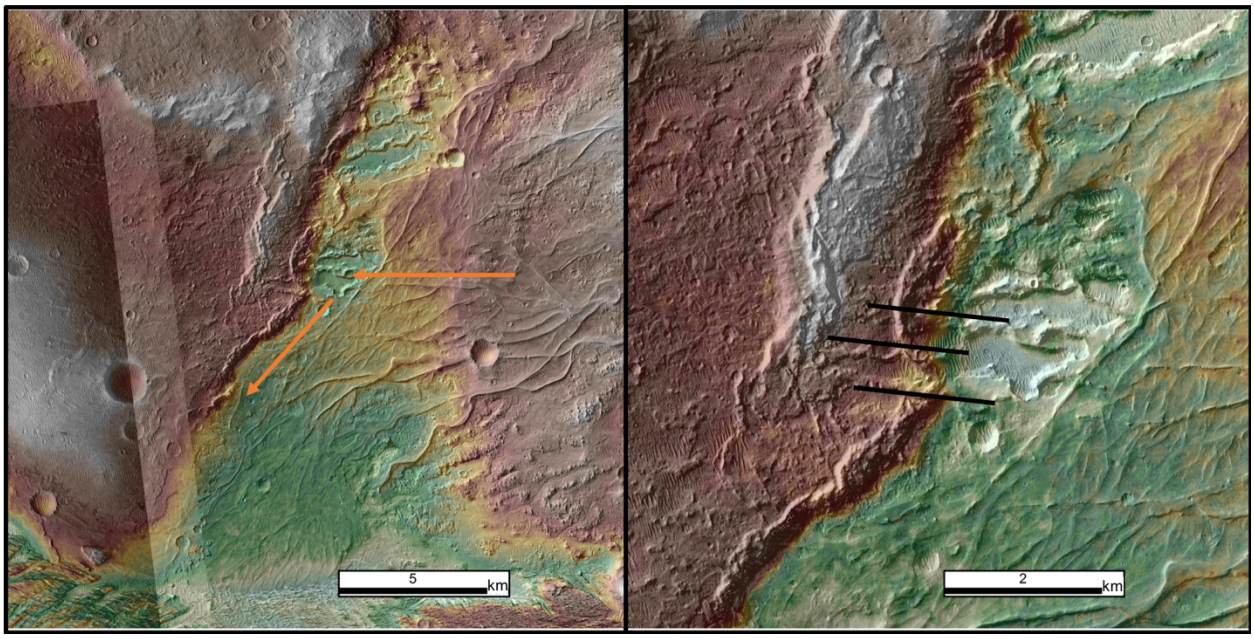


Figure 7: Images showing a wrinkle ridge deflecting an alluvial fan (left) and inverted fluvial deposits continuing across the same wrinkle ridge (right). Orange arrows show flow directions of alluvial fan deposit. Black lines show inverted fluvial deposits crosscutting a wrinkle ridge. This wrinkle ridge is located in the east central part of AD (#6). This figure is similar to one in Kite et al. (2015).

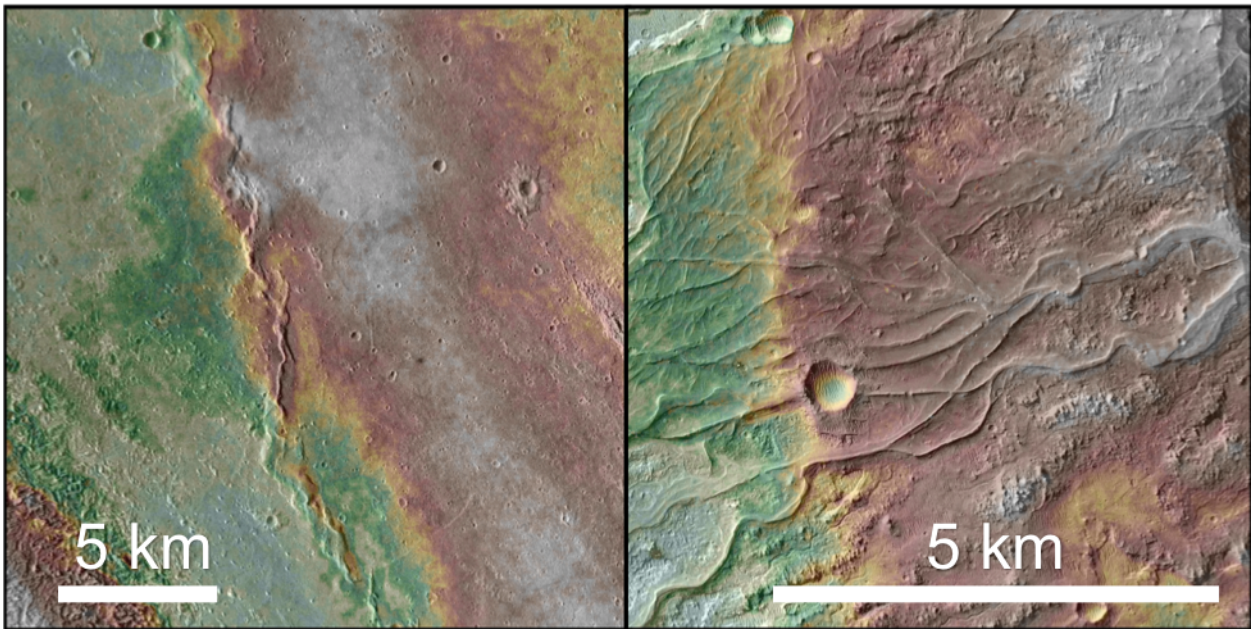


Figure 8: Comparison of AD wrinkle ridge #4 (left) and inverted channel in SE AD (right) morphology. Colors show elevation, with cool colors as low elevations and warmer colors as high elevations. Wrinkle ridges have a more crenulated, irregular ridge morphology, while the inverted channels have a smoother but more branching morphology. This is the same wrinkle ridge as Figure 1.

Table 2: Criteria for determining certainty levels of wrinkle ridges. These criteria are compiled from the literature on wrinkle ridges, using the most commonly mentioned morphologic characteristics.

Wrinkle Ridge Characteristics	**Certainty Level**		
	Certain	Probable	Possible
Profile View: **1. Topographic Rise** **2. Asymmetry**	2 of 2 profile view criteria needed	1 of 2 profile view criteria needed	1 of 2 profile view criteria needed
Map View: **1. Narrow ridge** **2. En échelon segments** **3. Curvilinear shape** **4. Broad arch**	3 of 4 map view criteria needed	3 of 4 map view criteria needed	2 of 4 map view criteria needed

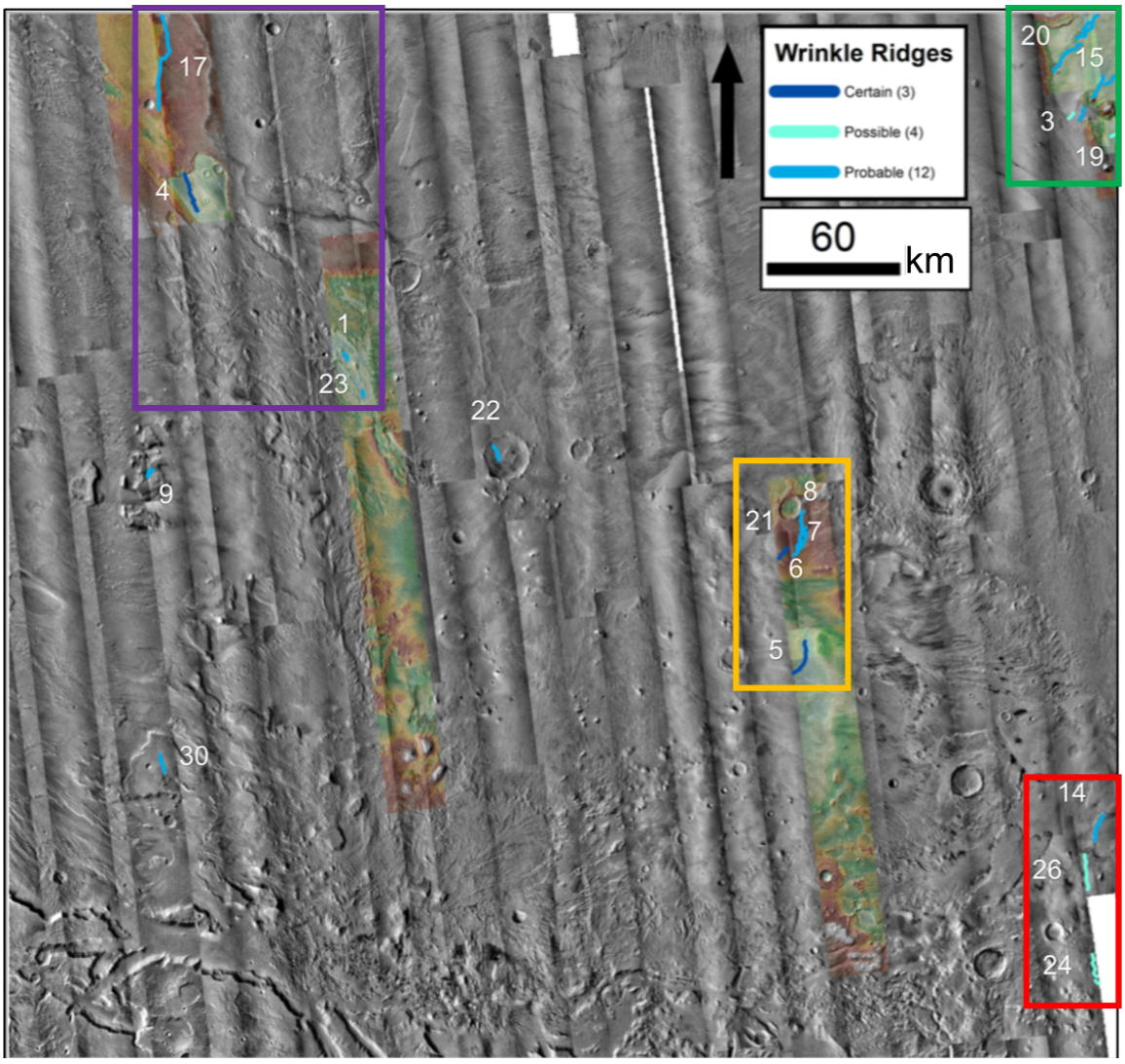


Figure 9: CTX mosaic of the AD mapping area showing all wrinkle ridges mapped as well as coverage by CTX DEMs. For the DEMs, colors indicate topographic elevation, with orange and brown as higher elevations and green as lower elevations. Colored boxes show geospatial groupings, or “clusters”, of wrinkle ridges.

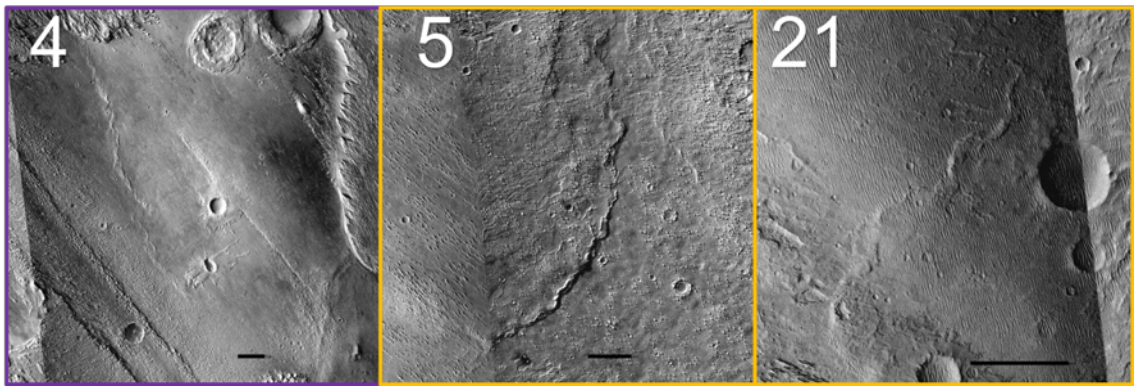


Figure 10: All wrinkle ridges mapped as Certain. All scale bars are 2 kilometers. Colored outlines match colored boxes indicating clusters from Figure 9.

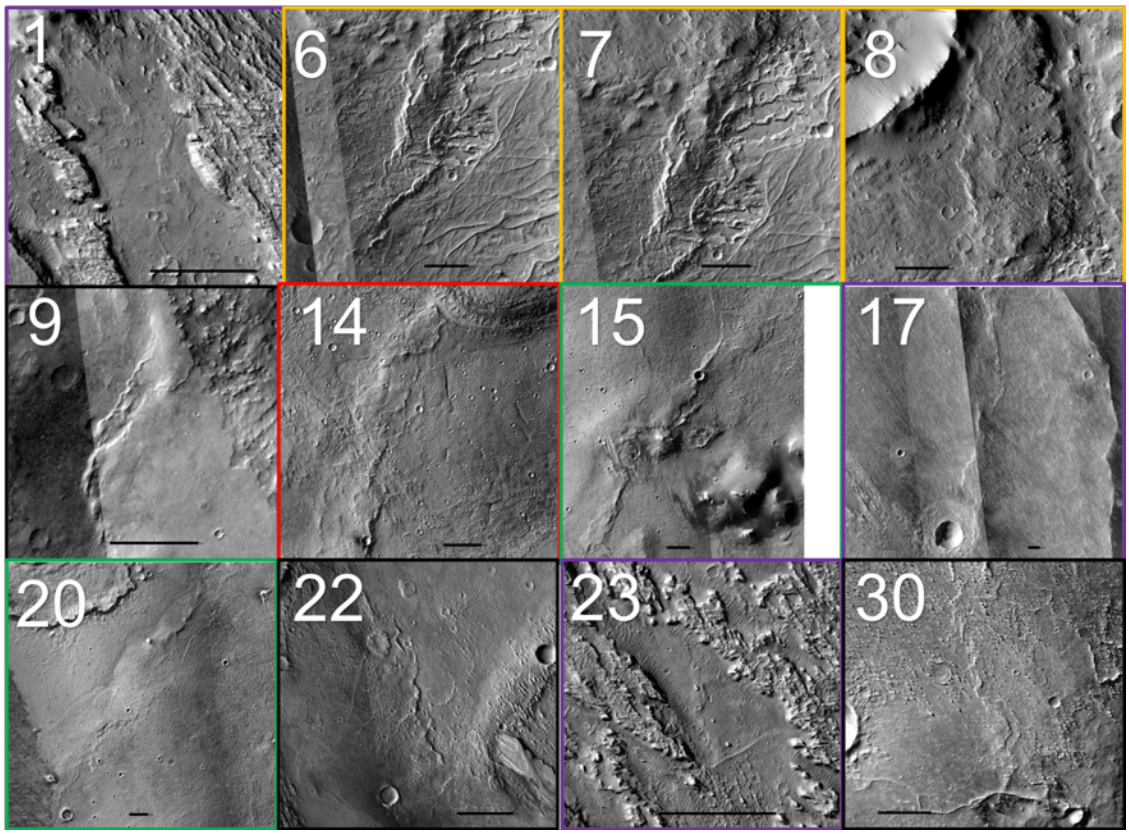


Figure 11: All wrinkle ridges mapped as Probable. All scale bars are 2 kilometers. Colored outlines match colored boxes indicating clusters from Figure 9 where applicable.

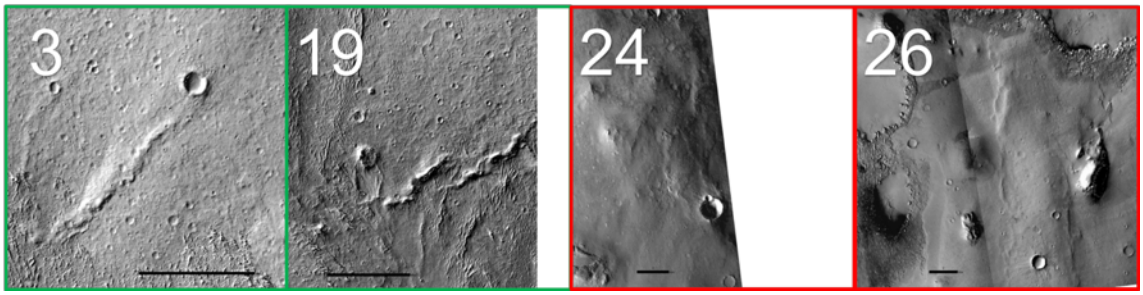


Figure 12: All wrinkle ridges mapped as Possible. All scale bars are 2 kilometers. Colored outlines match colored boxes indicating clusters from Figure 9.

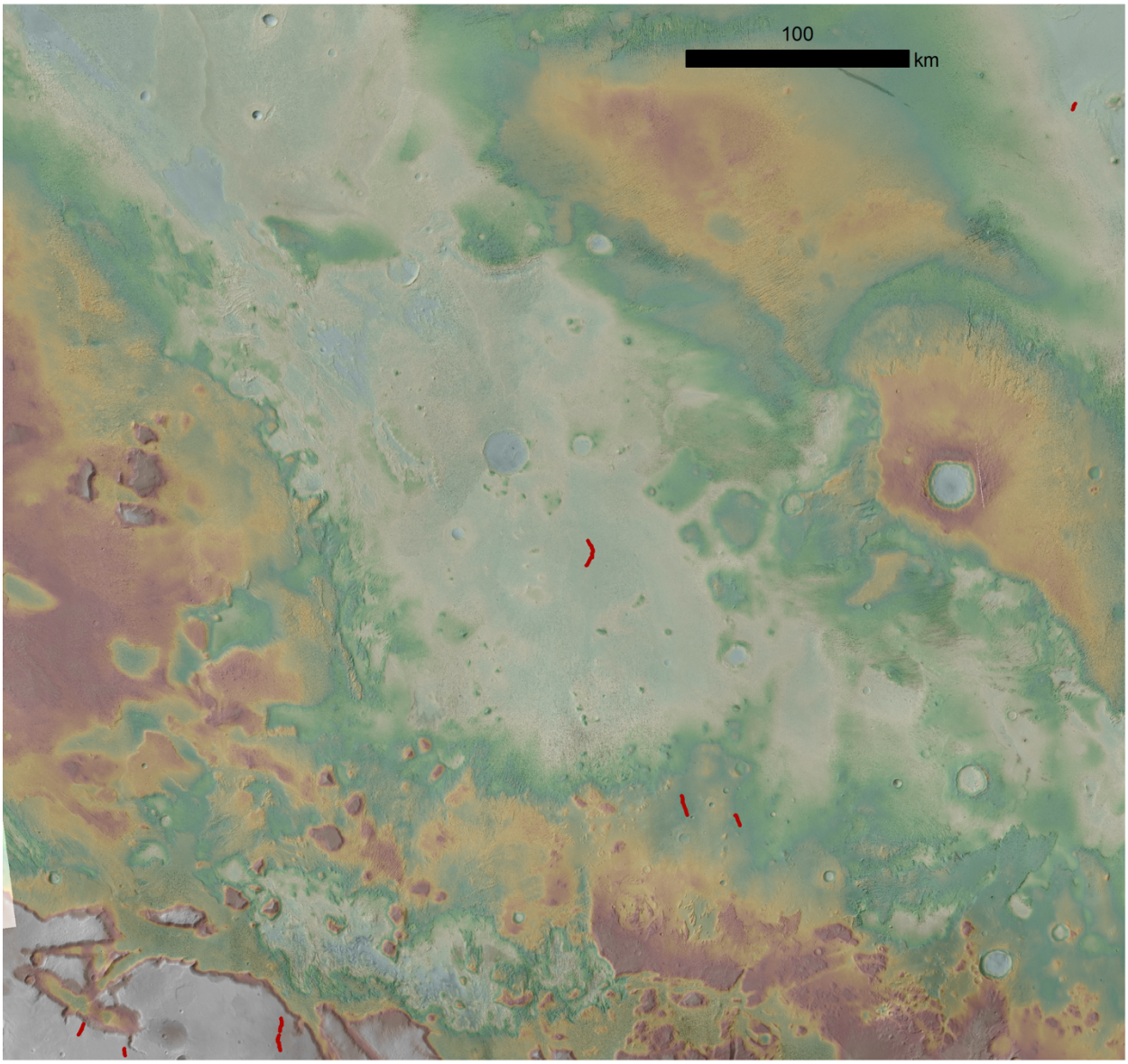


Figure 13: AD study area showing locations of ridges determined not to be wrinkle ridges. These ridges are shown as red lines. See Table 3 for exact coordinates of these ridges.

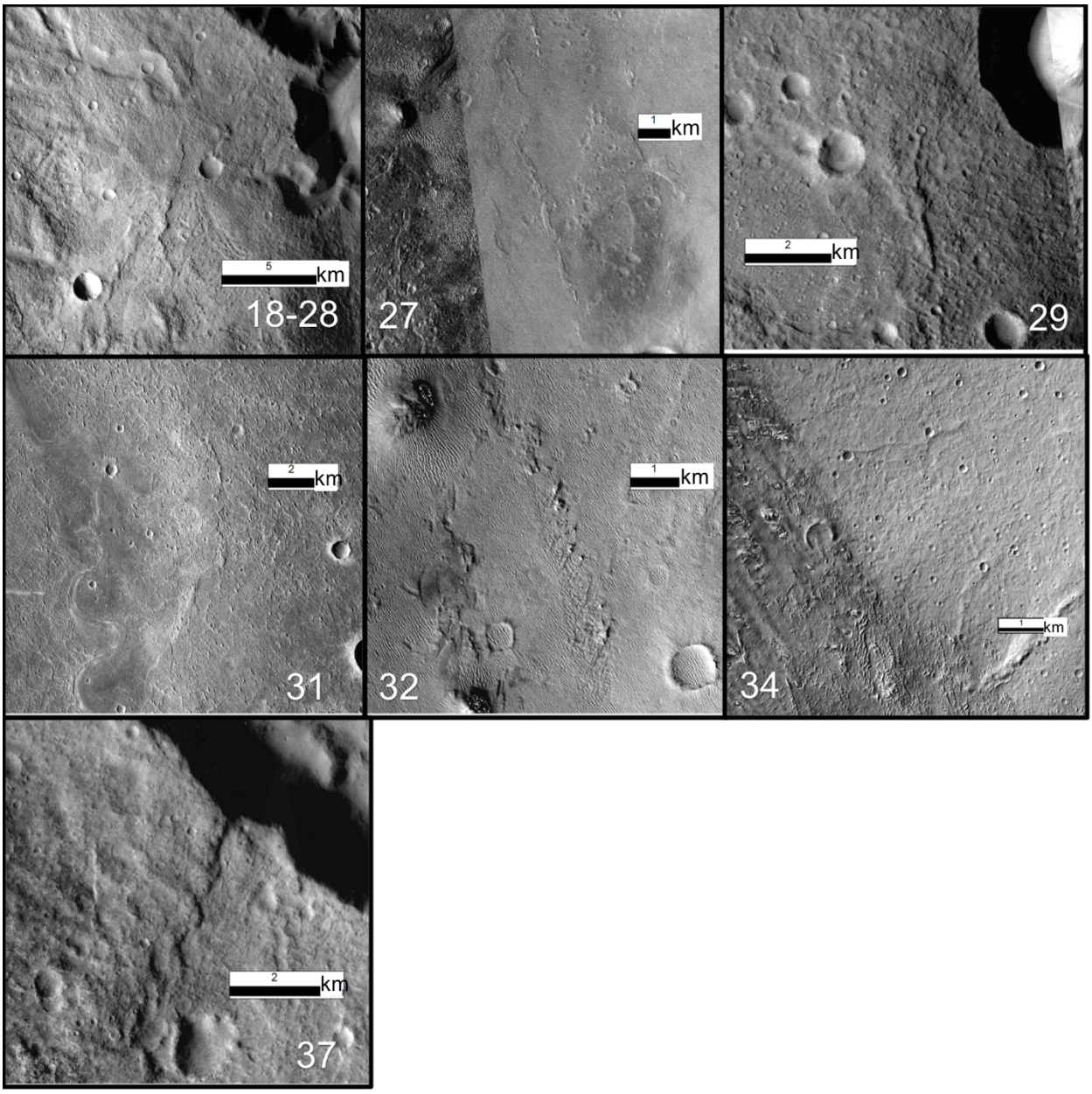


Figure 14: All ridges in AD determined not to be wrinkle ridges using the characteristics in Tables 2 and 3. Ridges 18 and 28 are in the same image due to close proximity to each other.

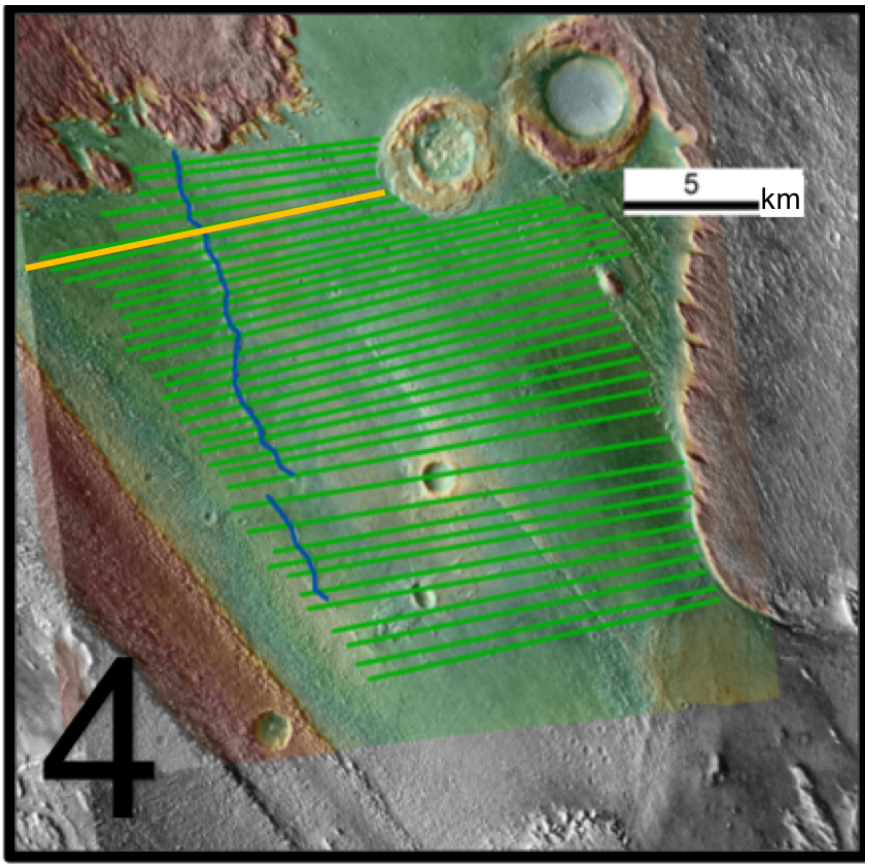


Figure 15: An illustration of topographic profile lines, shown here for wrinkle ridge #4. The mapped wrinkle ridge line follows the crest of the ridge, although the profile lines were made much wider to capture the width of the broad arch and topographic rise. Yellow line marks location of profile line #8, shown below. See the Appendix for the location of topographic profiles on the other 11 wrinkle ridges for which I was able to derive CTX stereo-pair DEM data.

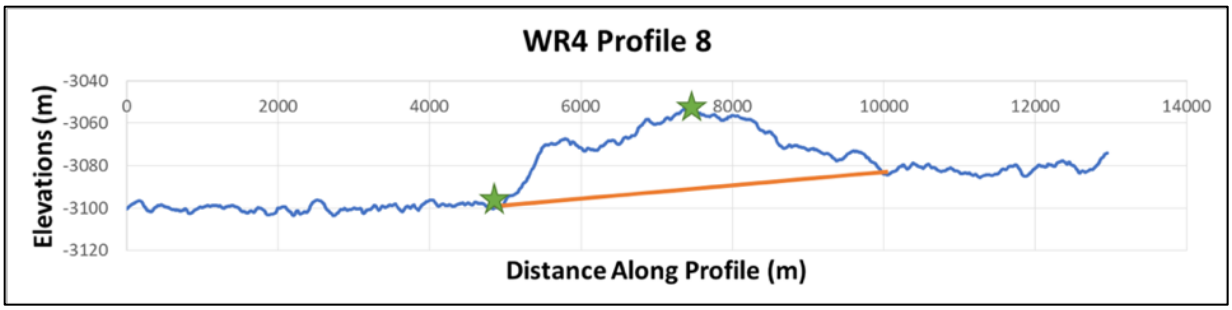


Figure 16: Graph of topographic profile #8 from Wrinkle Ridge #4. Orange line shows width measurement and green stars show lowest and highest points used for height measurement. The width for each ridge was measured as the straight line length between the point on either side of the ridge marking a change in slope. The height for each ridge was measured as the difference in elevation between the highest and lowest points on the ridge.

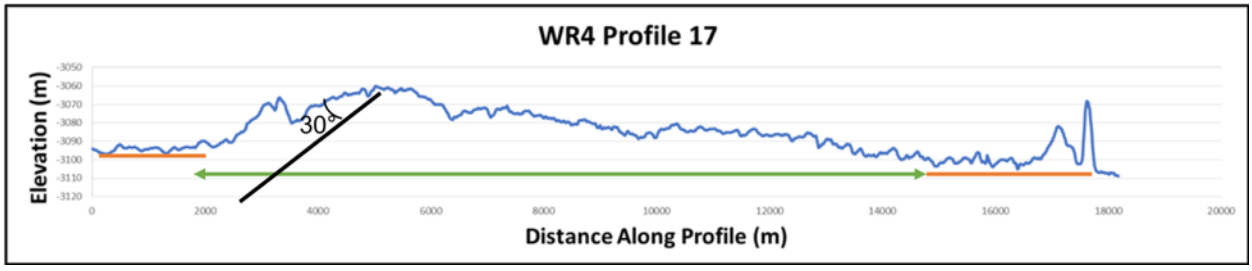


Figure 17: Example profile showing measurements used for shortening and strain calculations. Green line with arrows shows the measured straight-line width of the wrinkle ridge. The integrated length of the blue profile line is taken as the original width. The orange lines on either side of the wrinkle ridge mark the average elevation there; the difference between these two elevations is considered to be the elevation offset. The black line represents the assumed fault and fault dip underneath the ridge.

Table 3: Characteristics for each wrinkle ridge and the corresponding assigned certainty level, as well as characteristics of features originally mapped and then determined not to be wrinkle ridges (those without numbers).

WR #	Topogra-phic rise	Asymmetry	Broad arch	Narrow ridge	Curvi-linear shape	En échelon segments	Total profile view (first 2)	Total map view (last 4)	Certainty	Start X,Y	End X,Y
1	?	X	X	X	X	X	1	4	Probable	150.09°, -2.65°	150.06°, -2.6°
3		X	X	X			1	2	Possible	155.62°, -0.80°	155.66°, -0.77°
4	X	X	X	X		X	2	3	Certain	148.90°, -1.45°	148.85°, -1.23°
5	X	X	X	X	X		2	3	Certain	153.51°, -5.06°	153.60°, -4.81°
6		X	X	X	X		1	3	Probable	153.51°, -4.15°	153.61°, -3.98°
7		X	X	X	X		1	3	Probable	153.54°, -4.09°	153.61°, -3.94°
8		X	X	X		X	1	3	Probable	153.57°, -3.95°	153.58°, -3.82°
9		X	X	X	X		1	3	Probable	148.56°, -3.55°	148.57°, -3.50°
14	?	X	X	X		X	1	3	Probable	155.82°, -6.34°	155.89°, -6.14°
15	?	X	X	X		X	1	3	Probable	155.74°, -0.73°	155.99°, -0.47°
17		X	X	X		X	1	3	Probable	148.65°, -0.73°	148.67°, -0.02°
				X	X		0	2	Not	149.60°, -7.78°	149.61°, -7.68°
19	X			X		X	1	2	Possible	155.94°, -0.94°	156.00°, -0.91°
20		X	X	X	X	X	1	4	Probable	155.51°, -0.44°	155.84°, -0.02°
21	X	X	X	X	X		2	3	Certain	153.40°, -4.18°	153.46°, -4.09°
22		X	X	X		X	1	3	Probable	151.26°, -3.42°	151.21°, -3.31°
23	?	X	X	X	X		1	3	Probable	150.21°, -2.93°	150.21°, -2.89°
24		X	X	X			1	2	Possible	155.82°, -7.41°	155.80°, -7.21°
26		X	X	X			1	2	Possible	155.76°, -6.71°	155.74°, -6.45°
				X			0	1	Not	152.68°, -6.14°	152.64°, -6.00°

Table 3 Continued

WR #	Topogra-phic rise	Asymmetry	Broad arch	Narrow ridge	Curvilinear shape	En échelon segments	Total profile view (first 2)	Total map view (last 4)	Certainty	Start X,Y	End X,Y
				X	X		0	2	Not	149.60°, -7.93°	149.59°, -7.81°
				X	X		0	2	Not	148.43°, -7.97°	148.42°, -7.91°
30		X	X	X		X	1	3	Probable	148.66°, -5.68°	148.68°, -5.81°
				X	X		0	2	Not	151.93°, -4.07°	151.92°, -4.25°
						X	0	1	Not	153.08°, -6.22°	153.04°, -6.15°
				X	X		0	2	Not	155.60°, -0.80°	155.62°, -0.75°
				X		X	0	2	Not	148.07°, -7.81°	148.11°, -7.73°

Table 4: Wrinkle ridge orientations, certainty levels, locations, and dimensions. The height and width were measured for each profile across a ridge and the average value for each ridge is reported here. Estimated measurement error on height measurements is +/- 1 m, on width measurements is +/- 97 m, and on length measurements is +/- 362 m. N/A denotes wrinkle ridges for which no DEM was available.

WR #	Orientation	Certainty Level	Cluster or Location	Lithology	Height (m)	Width (m)	Length (m)
1	331	Probable	Northwest	Lava	17	839	3,067
4	345	Certain	Northwest	Lava	64	9,538	18,172
17	2	Probable	Northwest	Lava	141	5,562	46,027
23	349	Probable	Northwest	Lava	16	551	2,214
3	46	Possible	Northeast	Lava	N/A	N/A	3,207
15	44	Probable	Northeast	Lava	52	7,207	23,395
19	61	Possible	Northeast	Lava	47	4,939	3,983
20	38	Probable	Northeast	Lava	67	10,569	30,525
5	20	Certain	East Central	Sedimentary?	46	671	17,578
6	31	Probable	East Central	Sedimentary?	54	513	13,802
7	24	Probable	East Central	Sedimentary?	87	1,656	10,920
8	5	Probable	East Central	Sedimentary?	58	2,724	8,486
21	37	Certain	East Central	Sedimentary?	47	2,014	7,136
9	11	Probable	West Central Block	Highlands?	N/A	N/A	8,987
14	19	Probable	Southeast	Unknown	N/A	N/A	13,837
24	353	Possible	Southeast	Unknown	N/A	N/A	13,137
26	355	Possible	Southeast	Unknown	N/A	N/A	16,056
22	336	Probable	Central Crater	Unknown	N/A	N/A	6,568
30	349	Probable	Southwest Block	Highlands?	N/A	N/A	9,148

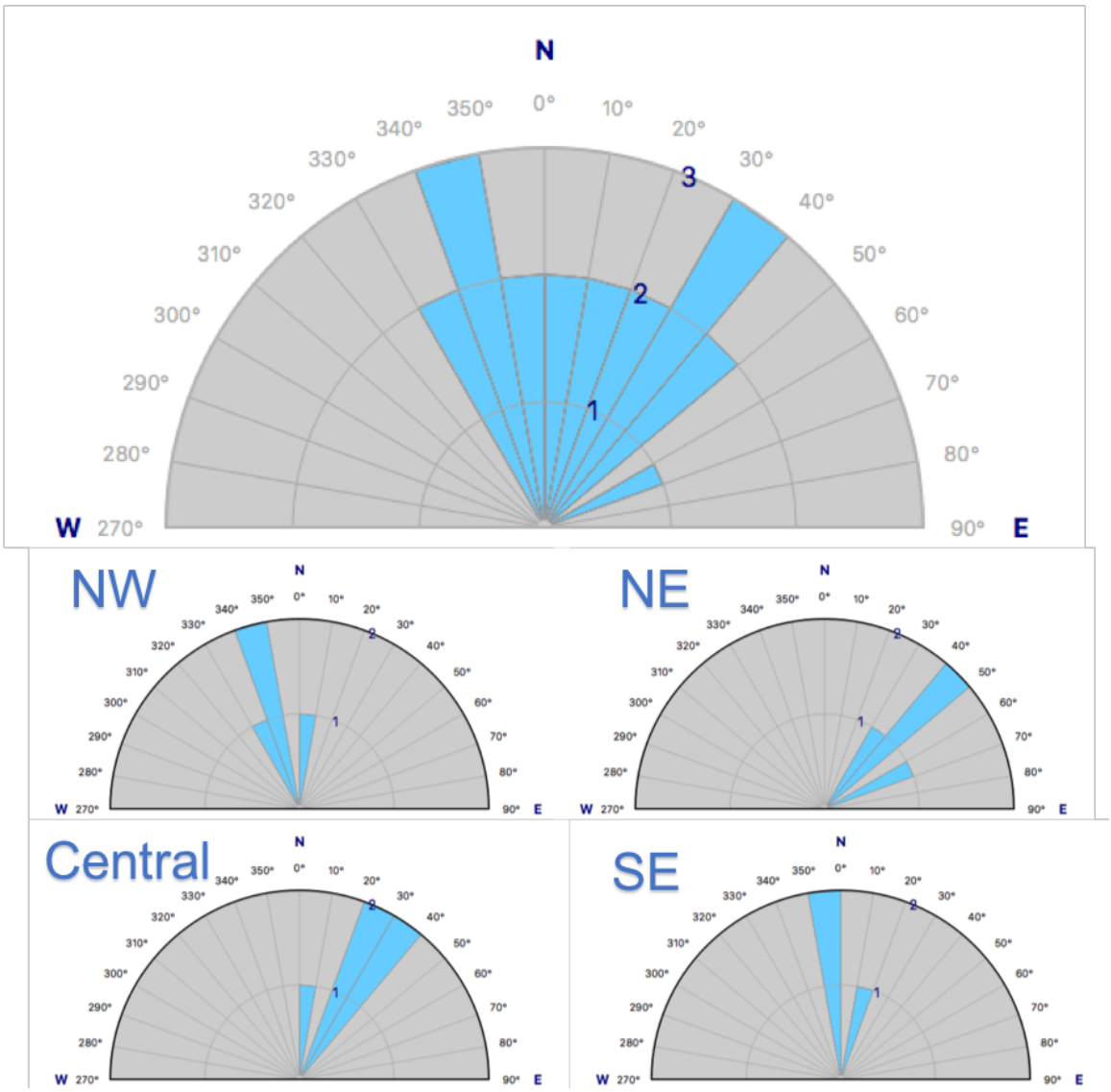


Figure 18: Rose diagram of all 19 wrinkle ridge orientations in AD, along with diagrams for the orientations of each geospatial cluster. Single-digit numbers on the concentric semi-circles of the diagram correspond to the number of wrinkle ridges within each 10º bin.

Table 5: Results for calculations of shortening and strain from folding. Shortening results are in meters. Shortening was calculated by subtracting the straight-line length across each ridge from the integrated length of topographic profiles across that ridge. Uncertainties were calculated by dividing the standard deviation of all shortening measurements for a ridge by the square root of the number of measurements.

WR#	**Shortening from folding (m)**	**Strain from folding**
1	3 ± 0	0.002
4	11 ± 1	0.001
5	13 ± 1	0.002
6	14 ± 1	0.004
7	15 ± 2	0.004
8	35 ± 7	0.008
15	7 ± 1	0.001
17	45 ± 2	0.004
19	5 ± 0	0.001
20	60 ± 5	0.003
21	6 ± 0	0.001
23	9 ± 3	0.008

Table 6: Results for calculations of shortening and strain from faulting. Shortening results are in meters. Shortening was calculated by dividing the elevation offset across a ridge by the tangent of the assumed fault dip (25º, 30º, or 35º, as indicated). Uncertainties were calculated by dividing the standard deviation of all shortening measurements for a ridge by the square root of the number of measurements.

WR #	**Shortening from faulting (m)**	**Strain from faulting**	**Shortening from faulting (m)**	**Strain from faulting**	**Shortening from faulting (m)**	**Strain from faulting**
	(25°)		**(30°)**		**(35°)**	
1	11 ± 2	0.006	9 ± 1	0.005	7 ± 1	0.004
4	30 ± 2	0.002	25 ± 2	0.002	20 ± 2	0.001
5	64 ± 6	0.010	52 ± 5	0.008	43 ± 4	0.007
6	63 ± 8	0.018	51 ± 6	0.014	42 ± 5	0.012
7	38 ± 7	0.011	31 ± 6	0.009	25 ± 5	0.007
8	68 ± 4	0.016	55 ± 3	0.013	45 ± 2	0.010
15	33 ± 4	0.003	27 ± 3	0.002	22 ± 2	0.002
17	176 ± 5	0.014	142 ± 4	0.012	117 ± 3	0.010
19	68 ± 5	0.007	55 ± 4	0.006	45 ± 3	0.005
20	28 ± 3	0.002	23 ± 3	0.001	19 ± 2	0.001
21	35 ± 5	0.009	28 ± 4	0.007	23 ± 3	0.006
23	17 ± 3	0.016	14 ± 2	0.013	11 ± 2	0.011

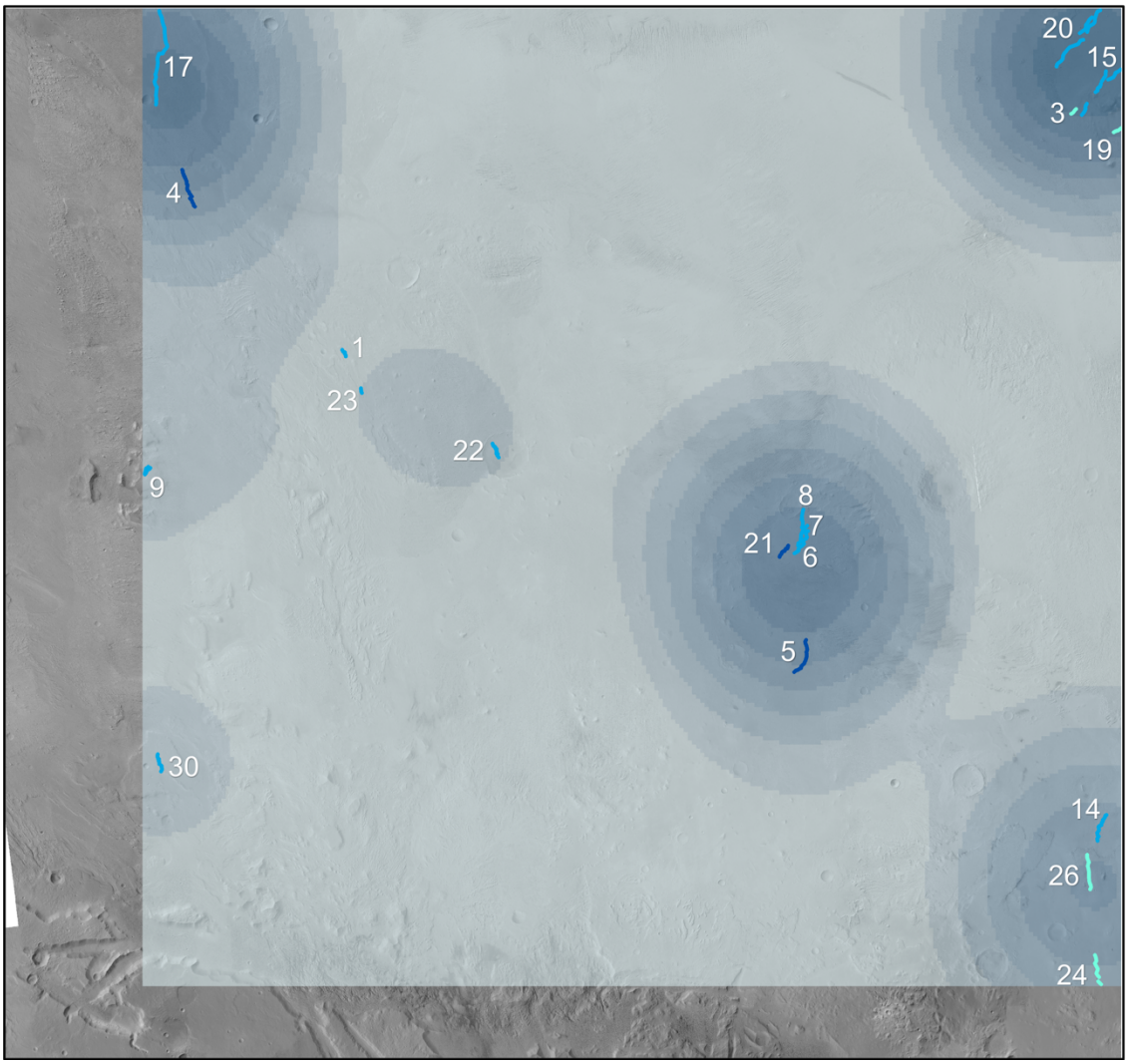


Figure 19: Heat map of wrinkle ridges made using Kernel Density tool in ArcMap. Darker blue colors mean there is a higher density of wrinkle ridges per area in that location.

Table 7: Average strain and standard deviation for geospatial clusters of wrinkle ridges in AD.

Cluster	Average strain from folding	SD1	Average strain from faulting	SD2
NW	0.015 (1.5%)	0.021	0.013 (1.3%)	0.008
NE	0.004 (0.4%)	0.003	0.006 (0.6%)	0.002
Central	0.017 (1.7%)	0.021	0.026 (2.6%)	0.009

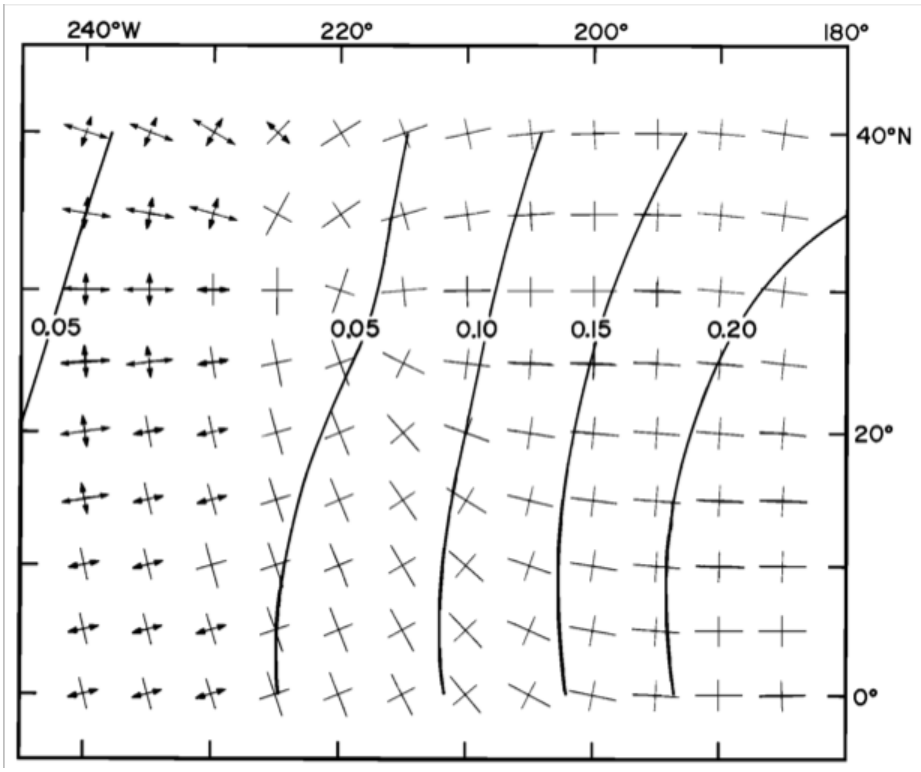


Figure 20: Figure 10 from Hall et al. (1986) showing a stress map of the area south of Elysium Mons based on an isostatic model of Tharsis from Banerdt et al. (1982). Crosses show horizontal principal stress directions, arrows indicate extension. Contours show maximum stress difference in kilobars.

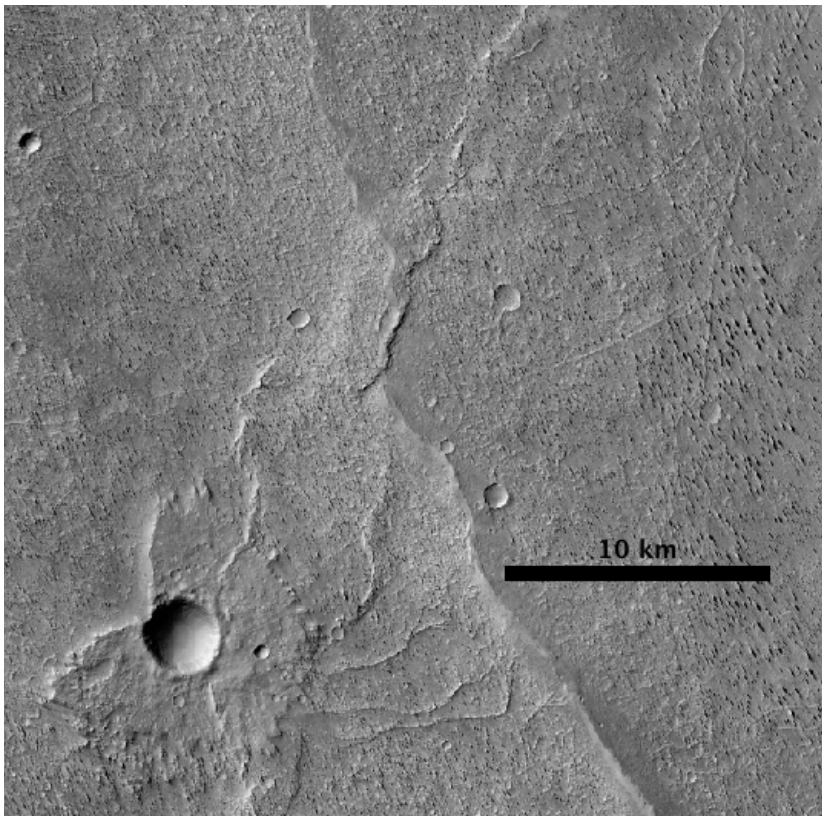


Figure 21: Image from just north of the AD study area showing WR 17 cutting across Aeolis Serpens (running from NW to SE across the image).

Vita

Rose Michelle Borden was born on July 30th, 1990 in Renton, WA. She grew up in Maple Valley, WA with her parents, Jon and Sara Borden, and eight younger siblings: Katie, Anna, Joshua, Melinda, Jon Andrew, Ruby, Michael, and Matthew. She was homeschooled until she graduated high school in June 2009. She then attended Green River Community College, graduating in December 2012 with an AAS degree in Early Childhood Education with a concentration in Special Education (Paraeducator). After working as a substitute paraeducator for one year, she decided to pursue a BS in Geology at Central Washington University. She graduated from CWU magna cum laude in December 2014, and then worked part-time as a nanny until summer 2015. In the fall of 2015 she started her graduate studies in the Earth and Planetary Sciences department at The University of Tennessee, Knoxville.